

APPLIED INFORMATION SYSTEMS RESEARCH (AISR) PROGRAM

First Annual Report for AISR Grant NNG06EC81I
Parallel-Processing Astrophysical Image-Analysis Tools
April 1, 2006 to March 30, 2007 (Year 1 of 3)

PI: Kenneth J. Mighell (National Optical Astronomy Observatory)

During the past year, the Principal Investigator (PI) has worked closely with *Spitzer Space Telescope's* Infrared Array Camera (IRAC) instrument team to demonstrate that his AISR-funded MATPHOT algorithm [1] for precision stellar photometry and astrometry can yield an improvement in the precision of stellar photometry obtained from IRAC Channel 1 (Ch1) observations of more than 100% over the best results obtained with aperture photometry and the state-of-the-art calibration procedures recommended in the Infrared Array Camera (IRAC) Data Handbook[2].

The PI presented the paper *Innovative image analysis software as a technology driver for advances in space telescope design*[3] on Wednesday May 31, 2006 at Space Telescopes and Instrumentation I: Optical, Infrared, and Millimeter (Conference 6265) of the SPIE International Symposium Astronomical Telescopes and Instrumentation 2006 (SPIE-Orlando) which was held in Orlando, Florida on May 24-31, 2006. In that paper, the presented *simulations* which indicated that by carefully modeling the image formation process within the IRAC Ch1 instrument using the MATPHOT algorithm, it might be possible to significantly improve the precision of IRAC Ch1 stellar photometry over the state-of-the-art reductions available at that time.

The PI presented the paper *Analysis of K-band imaging of the wide binary system σ CrB with the Lick Observatory NGS AO system*[4] on Thursday May 25, 2006 at SPIE-Orlando. In that paper, Mighell, Christou, and Drummond presented a MATPHOT-based analysis of near-infrared adaptive-optics observations of the astrometric calibrator σ Corona Borealis and showed that one can achieve excellent 2–3 milliarcsecond relative astrometry with short (0.057–10 sec) good-Strehl-ratio (reaching 50%) adaptive-optic observations in the K-band with a Brackett- γ filter ($\lambda_0 = 2.167 \mu\text{m}$; $\delta\lambda = 0.020 \mu\text{m}$).

The PI was the second author of the paper *Strehl ratio and image sharpness for Adaptive Optics*[5] which was presented on Monday May 29, 2006 at Advances in Adaptive Optics II (Conference 6272) at SPIE-Orlando. In that paper, Christou, Mighell, and Makidon present a detailed analysis of the relation between the Strehl ratio and various image sharpness metrics first proposed by Muller and Buffington [6].

Current infrared detector technology can produce imagers with non-uniform intrapixel response functions. Cameras based on such detectors can have large systematic errors in the measurement of the total stellar flux. Although this problem can be mitigated by oversampling the stellar image, many near-infrared cameras are undersampled in order to achieve a large field of view. The combination of undersampling stellar images with non-uniform detectors is currently diminishing

some of the potential science return of some infrared imagers onboard the *Hubble Space Telescope* and the *Spitzer Space Telescope*. Although the recorded flux and position of point sources is corrupted by using detectors with non-uniform intrapixel response functions, it is still possible to achieve excellent stellar photometry and astrometry — if the image formation process inside the detector is accurately modeled. A new analysis algorithm called the **Lost Flux Method** was developed by the PI and used to demonstrate how the precision of stellar photometry from an existing space-based near-infrared camera with a lossy detector can be significantly improved. Multiple observations of a single bright isolated star obtained with Channel 1 of the Spitzer Space Telescope Infrared Array Camera (IRAC) instrument were analyzed with the Lost Flux Method which yielded an improvement in photometric precision of more than 100% over the best results obtained with aperture photometry.

The Lost Flux Method was first presented to the space science community in the paper *Improving the Precision of Near-Infrared Stellar Photometry by Modeling the Image Formation Process within a Lossy Detector* [7] which was presented on Tuesday September 12, 2006 at the 2006 Advanced Maui Optical and Space Surveillance (AMOS) Technologies Conference which was held in Wailea, Maui, Hawaii on September 10-14, 2006.

The PI presented the paper *The Lost Flux Method: A New Algorithm for Improving the Precision of Space-Based Near-Infrared Stellar Photometry with Lossy Detectors* [8] on Monday October 16, 2007 at the Astronomical Data Analysis Software and Systems XVI which was held in Tucson, Arizona on October 15-18, 2006.

The PI presented poster #164.14 *The Lost Flux Method: A New Algorithm for Improving the Precision of Space-Based Near-Infrared Stellar Photometry with Lossy Detectors* [9] on Tuesday January 9, 2007 at the 209th meeting of the American Astronomical Society which was held at Seattle, WA on January 6-11, 2007.

The PI gave an invited hour-long lecture on the topic *Precision Stellar Photometry and Astrometry using Discrete Point Spread Functions: Theory and Practice* at the Department of Physics and Astronomy of the University of New Mexico, Albuquerque on December 1, 2006. This presentation discussed the theoretical and practical limits of precision stellar photometry and astrometry based on astrophysics and information theory. A PDF version of this PowerPoint presentation was submitted for possibly publication on the AISR website at <http://aisrp.nasa.gov/>; it is also available at <http://www.noao.edu/staff/mighell/2006DEC01/presentation.pdf>.

The PI has continued his very productive collaboration with Dr. Volodymyr Kindratenko, a Senior Research Scientist at the *National Center for Supercomputing Applications (NCSA)* at the University of Illinois at Urbana-Champaign. The article *Code Partitioning for Reconfigurable High-Performance Computing: A Case Study* [10] describes Dr. Kindratenko's efforts to port of MATPHOT's 21-pixel wide damped sinc interpolator (Equation 49 of [1]) to the FPGAs (Field Programmable Gate Arrays) of the SRC-6 MAPstation.

AISR-funded Publications from April 1, 2006 to March 30, 2007

- Innovative image analysis software as a technology driver for advances in space telescope design*, Mighell, K. J. 2006, in *Space Telescopes and Instrumentation I: Optical, Infrared, and Millimeter*, edited by J. C. Mather, H. A. MacEwen, and M. W. de Graauw, Proceedings of SPIE, Vol. 6265, 12 pages
- Analysis of K-band imaging of the wide binary system σ CrB with the Lick Observatory NGS AO system*, Mighell, K. J., Christou, J. C., & Drummond, J. D. 2006, in *Advances in Adaptive Optics II*, edited by B. L. Ellerbroek and D. B. Calia, Proceedings of SPIE, Vol. 6272, 6 pages
- Strehl ratio and image sharpness for Adaptive Optics*, Christou, J. C., Mighell, K. J., & Makidon, R. B. 2006, in *Advances in Adaptive Optics II*, edited by B. L. Ellerbroek and D. B. Calia, Proceedings of SPIE, Vol. 6272, 12 pages
- Improving the Precision of Near-Infrared Stellar Photometry by Modeling the Image Formation Process within a Lossy Detector*, Mighell, K. J. 2006, Proceedings of the 2006 Advanced Maui Optical and Space Surveillance (AMOS) Technologies Conference which was held in Wailea, Maui, Hawaii on September 10-14, 2006, pages 201-208
- The Lost Flux Method: A New Algorithm for Improving the Precision of Space-Based Near-Infrared Stellar Photometry with Lossy Detectors*, Mighell, K. J. 2006, ASP Conference Series: *Astronomical Data Analysis Software and Systems XVI*, edited by R. Shaw, F. Hill and D. Bell, 4 pages (in press)
- The Lost Flux Method: A New Algorithm for Improving the Precision of Space-Based Near-Infrared Stellar Photometry with Lossy Detectors*, Mighell, K. J. 2006, Bulletin of the American Astronomical Society, Vol. 38, page 1132 (poster # 164.14 at the 209th meeting of the AAS at Seattle, WA on 01/06-11/2007).

References

- [1] *Stellar Photometry and Astrometry with Discrete Point Spread Functions*,
Mighell, K. J. 2005,
MNRAS, 361, 861–878
- [2] *Infrared Array Camera Data Handbook (Version 3.0; January 20, 2006)*,
Reach, W. T., et al. 2006
[<http://ssc.spitzer.caltech.edu/irac/dh/iracdatahandbook3.0.pdf>]
- [3] *Innovative image analysis software as a technology driver for advances in space telescope design*,
Mighell, K. J. 2006,
in *Space Telescopes and Instrumentation I: Optical, Infrared, and Millimeter*,
edited by J. C. Mather, H. A. MacEwen, and M. W. de Graauw,
Proceedings of SPIE, Vol. 6265, 12 pages
- [4] *Analysis of K-band imaging of the wide binary system σ CrB with the Lick Observatory NGS AO system*,
Mighell, K. J., Christou, J. C., & Drummond, J. D. 2006,
in *Advances in Adaptive Optics II*,
edited by B. L. Ellerbroek and D. B. Calia,
Proceedings of SPIE, Vol. 6272, 6 pages
- [5] *Strehl ratio and image sharpness for Adaptive Optics*,
Christou, J. C., Mighell, K. J., & Makidon, R. B. 2006,
in *Advances in Adaptive Optics II*,
edited by B. L. Ellerbroek and D. B. Calia,
Proceedings of SPIE, Vol. 6272, 12 pages
- [6] *Real-time correction of atmospherically degraded telescope images through image sharpening*,
Muller, R. A., & Buffington, A. 1974,
J. Opt. Soc. Am., 64, 9, 1200-1211
- [7] *Improving the Precision of Near-Infrared Stellar Photometry by Modeling the Image Formation Process within a Lossy Detector*,
Mighell, K. J. 2006,
Proceedings of the 2006 Advanced Maui Optical and Space Surveillance (AMOS) Technologies Conference which was held in Wailea, Maui, Hawaii on September 10-14, 2006, pages 201-208
- [8] *The Lost Flux Method: A New Algorithm for Improving the Precision of Space-Based Near-Infrared Stellar Photometry with Lossy Detectors*,
Mighell, K. J. 2006,
ASP Conference Series: Astronomical Data Analysis Software and Systems XVI, edited by R. Shaw, F. Hill and D. Bell, 4 pages (in press)

- [9] *The Lost Flux Method: A New Algorithm for Improving the Precision of Space-Based Near-Infrared Stellar Photometry with Lossy Detectors*,
Mighell, K. J. 2006,
Bulletin of the American Astronomical Society, Vol. 38, page 1132
(poster # 164.14 at the 209th meeting of the AAS at Seattle, WA on 01/06-11/2007).
- [10] *Code Partitioning for Reconfigurable High-Performance Computing: A Case Study*,
Kinratenko, V. 2006,
in Proceedings of The International Conference on Engineering of Reconfigurable Systems and Algorithms (ERSA'06) which was held in Las Vegas, Nevada on June 26-29, 2006, 7 pages

Innovative Image Analysis Software as a Technology Driver for Advances in Space Telescope Design

Kenneth J. Mighell^a

^aNational Optical Astronomy Observatory, 950 N. Cherry Ave., Tucson, AZ 85719, U.S.A.

ABSTRACT

Innovative image analysis software has the potential to act as a technology driver for advancing the state-of-the-art in the design of space telescopes and space-based instrumentation. Total mission costs can sometimes be significantly reduced by using innovative compact optical designs that create ugly Point Spread Functions. Most traditional astronomical image analysis techniques, like precision stellar photometry and astrometry, were developed for the analysis of ground-based image data and many photometric reduction codes cleverly take full advantage of the blurring caused by the Earth's atmosphere. Image data from space-based cameras, however, is typically characterized by having significant amounts of power at high spatial frequencies. Mission designers have a penchant to approve of optical designs that are undersampled. Although excellent justifications can often be made for using complex optical designs that have ugly Point Spread Functions (e.g., reduced total mission cost) or for using detectors that are too big at a given wavelength (e.g., giving a wider field-of-view), the analysis of resultant image data from these designs is frequently problematical. Reliance upon traditional ground-based image analysis codes may preclude the use of innovative space-based optical designs if such designs are rejected during the design review process for the very practical reason that there is no proven way to accurately analyze the resultant image data. I discuss ongoing research efforts to develop new image analysis algorithms specifically for space-based cameras that may help NASA and ESA to enhance the scientific returns from future astrophysical missions while possibly lowering total mission costs.

Keywords: stellar photometry, astrometry, infrared detectors, Spitzer Space Telescope, IRAC, MATPHOT

1. CAN YOU FIT A BANANA?

Since the early 1990s, NASA's astrophysical mission designers have been challenged by administrators to do more science with fewer dollars. The "faster-better-cheaper" approach of mission design has led to many innovative mission concepts which achieve lower total mission cost at the price of having some distortion in the optical design of instruments and/or telescopes. One way of compensating for distorted optics is to do more image processing with clever analysis algorithms.

Technology Readiness Level¹ (TRL) enhancement programs at NASA, like the *Applied Information Systems Research* (AISR) program of NASA's Science Mission Directorate, can significantly help NASA's astrophysical mission designers by promoting the development of new image processing algorithms from a basic technology research level (e.g., TRL 1–3) to the point where mission designers can consider using these new image processing algorithms in future NASA missions (e.g., TRL 5–6). Space-based demonstration of new technologies is clearly beyond the scope and means of the AISR program, yet AISR can develop new applied information systems technologies which would be excellent candidates for consideration for use in demonstrator programs like the *New Millennium Program*² (NMP) which tests advanced technology for use in space flight.

One of the early design concepts for the 8-m *Next Generation Space Telescope* (NGST), currently known as the 6.5-m *James Webb Space Telescope* (JWST), had a very elliptical primary mirror in order to fit it into a 4-m diameter launch shroud. John Mather, the NGST Project Scientist, described this concept to me at the 193rd meeting of the American Astronomical Society (AAS) in January 1999 in Austin, Texas. He explained that one of the problems associated with the elliptical primary mirror design was the fact that the oddly shaped primary mirror would cause stars to be shaped like bananas. He then asked me: "Can you fit a banana?" I replied: "Yes." Since there was as yet no clear consensus within the NGST project in 1999 whether accurate stellar photometry and astrometry was theoretically and/or practically possible with very complex Point Spread Functions (PSFs), he replied: "Prove it!"

Through funding provided by the AISR program, I have met Mather's challenge by demonstrating that precise and accurate stellar photometry and astrometry is possible and practical with ugly space-based PSFs which have high spatial frequencies rarely seen in ground-based astronomy due to the blurring of the Earth's atmosphere.

Section 2 describes the role of Point Response Functions (PRFs) in the image formation process. An information-theory based point-source photometric and astrometric performance model which can be used to measure the measurement efficiency of stellar photometric reduction codes is outlined in Section 3. The key features of my MATPHOT algorithm, for precision stellar photometry and astrometry with discrete (sampled) PSFs, are described in Section 4. Problems related to doing astrophysical imaging with ugly (imperfect) detectors with large intrapixel quantum efficiency (QE) variations is presented in Section 5. A practical example is given in Section 6 where a theoretical analysis indicates that the current 5% stellar photometry precision limit from Channel 1 of *Spitzer Space Telescope's* Infrared Array Camera (IRAC) may be significantly improved in the near future through better modeling of the image formation process within the detector. Concluding remarks are given in Section 7.

2. POINT RESPONSE FUNCTIONS

A Point Response Function (PRF), Ψ , is the convolution of a Point Spread Function (PSF), ϕ , and a Detector Response Function (DRF), Λ :

$$\Psi \equiv \phi * \Lambda . \quad (1)$$

The PSF describes the two-dimensional distribution of *photons* from a star *just above the detector*. Although stellar photons are distributed as a point source above the Earth's atmosphere, a stellar image becomes a two-dimensional distribution as the stellar photons are scattered by atmospheric turbulence. The blurred stellar image is then further degraded by passage of the stellar photons through the combined telescope and camera optical elements (such as mirrors, lenses, apertures, etc.). The PSF is the convolution of all these blurring effects on the original point-source stellar image. The DRF is a two-dimensional discrete (sampled) function that describes how the detector electronics convert stellar photons (γ) to electrons (e^-) — including such effects as the diffusion of electrons within the detector substrate or the reflection (absorption) of photons on (in) the gate structures of the detector electronics.

A perfect DRF gives a PRF that is a *sampled version* of the PSF:

$$\Psi_i \equiv \int_{x_i-0.5}^{x_i+0.5} \int_{y_i-0.5}^{y_i+0.5} \phi(x, y) dx dy , \quad (2)$$

where i^{th} pixel (px) of the PRF located at (x_i, y_i) is the volume integral of the PSF over the area of the i^{th} pixel. The actual limits of the above volume integral reflect the appropriate mapping transformation of the x and y coordinates onto the CCD pixel coordinate system.

The **sharpness** of a PRF is defined as the volume integral of the *square* of the *normalized* PRF:

$$\text{sharpness} \equiv \iint_{-\infty}^{+\infty} \tilde{\Psi}^2 dx dy \equiv \iint_{-\infty}^{+\infty} \left(\frac{\Psi}{V} \right)^2 dx dy , \quad (3)$$

where V is the volume integral of the PRF, which has a value between one and zero. Physically, **sharpness** is a shape parameter which describes the “pointiness” of a PRF; **sharpness** values range from a maximum of one (all of the stellar flux is found within a single pixel) to a minimum of zero (a flat stellar image). For example, cameras that are out of focus have broad PSFs with **sharpness** values near zero. A normalized Gaussian³ PSF with a standard deviation of \mathcal{S} pixels that has been *oversampled* with a perfect DRF will have a **sharpness** value of $1/4\pi\mathcal{S}^2$. A critically-sampled normalized Gaussian PRF has a **sharpness** of $1/(4\pi)$ and any PRF with a **sharpness** value greater than that value (~ 0.0796) can be described as being undersampled. Diffraction limited optics, theoretically, give **sharpness** values that decrease (i.e., PSFs become flatter) with increasing photon wavelength — for a fixed pixel (detector) size. With real astronomical cameras, the value of **sharpness** frequently depends on *where the center of a star is located within the central CCD pixel* of the stellar image. For example, the *Hubble*

Space Telescope (HST) WFPC2 Planetary Camera PRF at a wavelength of 200 nm has an observed sharpness value of 0.084 if the PRF is centered in the middle of a PC pixel or 0.063 if the PRF is centered on a pixel corner (Table 6.5 of Ref. 4); at 600 nm the observed sharpness values range from 0.066 (pixel-centered) to 0.054 (corner-centered). The Wide-Field Cameras of the *HST* WFPC2 instrument have pixels which are approximately half the angular resolution of the PC camera pixels; stellar images on the WF cameras are undersampled and the observed range of WF camera sharpness values are 0.102–0.120 at 200 nm and 0.098–0.128 at 600 nm.

The *effective-background area*, β , of a PRF is defined as the *reciprocal* of the volume integral of the *square* of the PRF. Alternatively, the effective-background area (a.k.a. *equivalent-noise area*⁵ or *effective solid angle*) of a PRF is equal to the reciprocal of the product of its sharpness and the square of its volume:

$$\beta \equiv \left[\iint_{-\infty}^{+\infty} \Psi^2 dx dy \right]^{-1} = \frac{1}{V^2 \text{sharpness}}. \quad (4)$$

The effective-background area of a normalized Gaussian PRF is $4\pi\mathcal{S}^2$ px, where \mathcal{S} is the standard deviation in pixels; a critically-sampled normalized Gaussian PRF has an effective-background area of $4\pi \approx 12.57$ px. King⁵ notes that numerical integration of a realistic ground-based stellar profile gives an effective-background area of $30.8\mathcal{S}^2$ instead of the value of $4\pi\mathcal{S}^2$ for a normalized Gaussian profile.

3. PHOTOMETRIC AND ASTROMETRIC PERFORMANCE MODEL

Consider a CCD observation of single isolated star on a flat sky background. Assuming one already knows the PRF of the observation at the location of the star, a simple model of the observation would have just two parameters: the stellar intensity (\mathcal{E}) in electrons, and the observed background sky level (\mathcal{B}) in electrons. The observational model for the i^{th} pixel would be

$$m_i \equiv \mathcal{B} + \mathcal{E}V\tilde{\Psi}_i, \quad (5)$$

where V is the volume integral of the PRF and $\tilde{\Psi}_i$ is the value of the i^{th} pixel of the *normalized* PRF ($\tilde{\Psi}_i \equiv \Psi_i/V$).

I have developed a realistic point-source photometric performance model for CCD PSF-fitting stellar photometric reduction codes.⁶ The theoretical *upper limit* for the photometric signal-to-noise ratio (S/N) of CCD PSF-fitting stellar photometric algorithms is

$$\text{S/N} \equiv \frac{\mathcal{E}}{\sigma_{\mathcal{E}}} \approx \frac{\mathcal{E}}{\sqrt{\frac{\mathcal{E}}{V} + \beta \left(1 + \sqrt{\beta/N}\right)^2 [\mathcal{B} + \sigma_{\text{RON}}^2]}}, \quad (6)$$

where β is the effective-background area of the PRF and σ_{RON} is the rms CCD readout noise. These approximations assume, for the sake of simplicity, that any noise contribution due to dark current and quantization noise is negligible. While these additional noise sources can be added to create an even more realistic performance model for stellar photometry, the assumption of low dark current and minimal quantization noise is realistic for state-of-the-art astronomical-grade CCD imagers. This photometric performance model has bright and faint star limits⁶ which are the same, respectively, as the bright and faint star Cramér-Rao Lower Bounds for stellar photometry imaged with a perfect noiseless detector.^{5,7} The resulting photometric error is approximately

$$\Delta\text{mag} \approx \frac{1.0857}{\text{S/N}}, \quad (7)$$

where the constant 1.0857 is an approximation for Pogson's⁸ ratio $a \equiv 5/\ln(100) = 2.5\log(e)$.

I have developed a realistic point-source astrometric performance model for CCD PSF-fitting stellar photometric reduction codes.⁶ The theoretical *lower limit* of the rms measurement error for the stellar position in the x coordinate (\mathcal{X}) for a single isolated star on a flat sky is

$$\sigma_{\mathcal{X}} \approx \sqrt{\frac{\mathcal{L}^2}{\mathcal{E}V} \left[1 + 8\pi (\mathcal{B} + \sigma_{\text{RON}}^2) \frac{\mathcal{L}^2}{\mathcal{E}V} \right]}, \quad (8)$$

where

$$\mathcal{L} \equiv \sqrt{\frac{\beta V^2}{4\pi}} = \frac{1}{\sqrt{4\pi \text{ sharpness}}} \quad (9)$$

is the *critical-sampling scale length* of the PRF* in pixel units. The rms stellar position measurement error in the y coordinate (\mathcal{Y}) is the same, by symmetry, as for \mathcal{X} : $\sigma_{\mathcal{Y}} = \sigma_{\mathcal{X}}$. The critical-sampling scale length of a critically-sampled PRF imaged with a perfect detector, by definition, is one pixel; $\mathcal{L} > 1$ indicates that the PRF is *oversampled*, while $\mathcal{L} < 1$ indicates that the PRF is *undersampled*.

This astrometric performance model has bright and faint star limits⁶ which are the same, respectively, as the bright and faint star Cramér-Rao Lower Bounds for stellar astrometry of a single isolated Gaussian star on a flat sky background imaged with a perfect noiseless detector with infinitely small pixels (a.k.a. the *photonic limit*).⁷ The Cramér-Rao Lower Bound for stellar astrometry of a single isolated Gaussian star on a flat sky background imaged with a perfect noiseless CCD *with square pixels*⁹ quickly approaches the photonic limits with *well-sampled* observations; undersampled observations will have larger astrometric errors than predicted by the photonic limits.

4. PHOTOMETRY & ASTROMETRY WITH DISCRETE PSFS

I have developed a C-language implementation¹⁰ of my MATPHOT algorithm^{6,11,12} for precise and accurate stellar photometry and astrometry with discrete Point Spread Functions (PSFs). The MATPHOT code uses discrete (sampled) Point Spread Functions consisting of a numerical table represented by a matrix in the form of a FITS¹³ image. Discrete PSFs are shifted within an observational model using a 21-pixel-wide damped sinc function,

$$f^{\text{shifted}}(x_0) \equiv \sum_{i=-10}^{10} f(x_i) \frac{\sin(\pi(x_i - x_0))}{\pi(x_i - x_0)} \exp\left(-\left[\frac{x_i - x_0}{3.25}\right]^2\right), \quad (10)$$

and position partial derivatives are computed using a five-point numerical differentiation formula,

$$f'(x_i) \approx \frac{1}{12} [f(x_{i-2}) - 8f(x_{i-1}) + 8f(x_{i+1}) - f(x_{i+2})]. \quad (11)$$

Precise and accurate stellar photometry and astrometry are achieved with undersampled CCD observations by using supersampled discrete PSFs that are sampled 2, 3, or more times more finely than the observational data. Although these numerical techniques are not mathematically perfect, they are sufficiently accurate for precision stellar photometry and astrometry due to photon noise which is present in all astronomical imaging observations.⁶ The current implementation¹⁰ of the MATPHOT algorithm is based on a robust implementation^{11,14} of the Levenberg¹⁵-Marquardt¹⁶ method of nonlinear least-squares minimization. Detailed analysis of simulated *Next Generation Space Telescope* (NGST) observations demonstrate that millipixel relative astrometry and millimag photometric precision is achievable with complicated space-based discrete PSFs.⁶

A simulated NGST V-band stellar observation with the 8-meter TRW-concept 1.5-micron diffraction-limited primary mirror is shown in Fig. 1 with the 90%, 50%, 10%, 1%, and 0.1% contours relative to the peak intensity. The pixel scale is 0.0128 arcsec pixel⁻¹. The original version of this PSF was kindly provided by John Krist (STScI, now at JPL). The right side of Fig. 1 shows the MATPHOT-based analysis of 10,000 simulated NGST V-band CCD observations of stars with true flux values between 250 and 10⁶ electrons (photons). Each observation was simulated with a 2×2 supersampled NGST PSF located near the center of 60×60 pixels on a flat background of 100 electrons (e⁻) with a CCD readout noise level of 3 e⁻ pixel⁻¹. The results are plotted using box-and-whisker plots⁶ to better display the statistical range of recovered values for photometry and astrometry. Fig. 2 shows similar results for simulated 6.5-m *James Webb Space Telescope* (JWST) observations with a perfect one-micron PSF (shown with a log stretch to better display the higher spatial frequencies). The solid curves in Figs. 1 and 2 show the predicted median performance of the MATPHOT algorithm for these simulations;

*From the definition of the effective-background area of an oversampled Gaussian PRF with a standard deviation of \mathcal{S} pixels and $V < 1$, $\beta_{\mathcal{G}} \equiv 4\pi\mathcal{S}^2/V^2$, one sees that critical-sampling scale length has been designed to be a proxy for \mathcal{S} for *any* PRF.

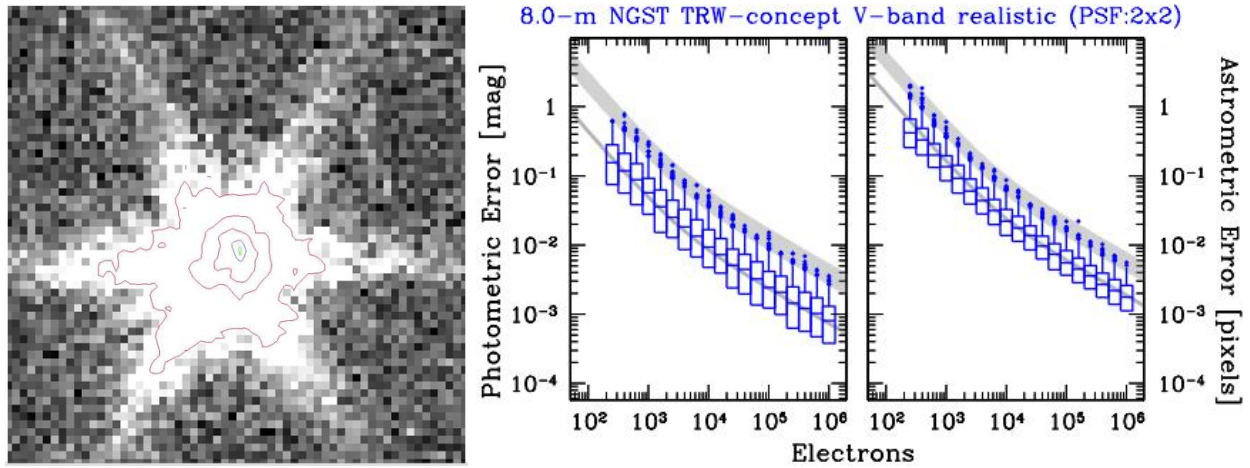


Figure 1. MATPHOT analysis of 10,000 simulated NGST stellar observations.

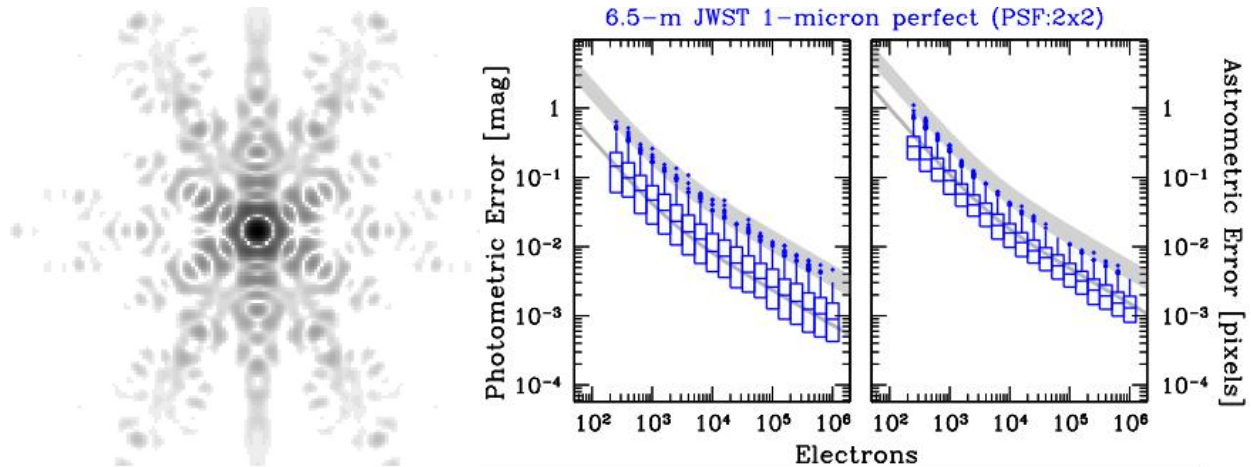


Figure 2. MATPHOT analysis of 10,000 simulated JWST stellar observations.

note that the actual median values (central bars in the boxes) lie on top or very near the performance model prediction. The wide bands in the above photometric (astrometric) error plots show the predicted outlier region for 2.3σ (3.0σ) to 5.0σ outliers (shown as points above the top whisker in Figs. 1 and 2). Note how well the theoretical performance model agrees with the actual MATPHOT measurements — even with these very complicated (simulated) space-based discrete PSFs.

5. UGLY DETECTORS

Current infrared detector technology can produce imagers with non-uniform pixel response functions. Lauer¹⁷ reported peak-to-peak variation of 0.39 mag at the J band (F110W) and 0.22 mag at H band (F160W) of the NIC3 camera of the *HST* NICMOS instrument. The peak-to-peak variation of 0.2 mag at F160W with NIC3 has been independently verified.¹⁸ Significant flux loss due to non-uniform intrapixel pixel response functions is clearly an observational fact in some existing space-based astronomical cameras.

An experimental version of the MATPHOT demonstrator program, called MPDX,⁶ was created to simulate such an IR detector; a pixel was split into 16 subpixels and all the subpixels in the first row and column were declared to be gate structures with zero efficiency converting photons to electrons and the other nine subpixels had 100% conversion efficiency. Note that only 56% of the total pixel area was optically active.

Ten thousand undersampled CCD stellar observations of -15 mag stars (10^6 electrons) were simulated and analyzed with MPDX using a 4×4 supersampled version of the simulated V-band NGST PSF described above.

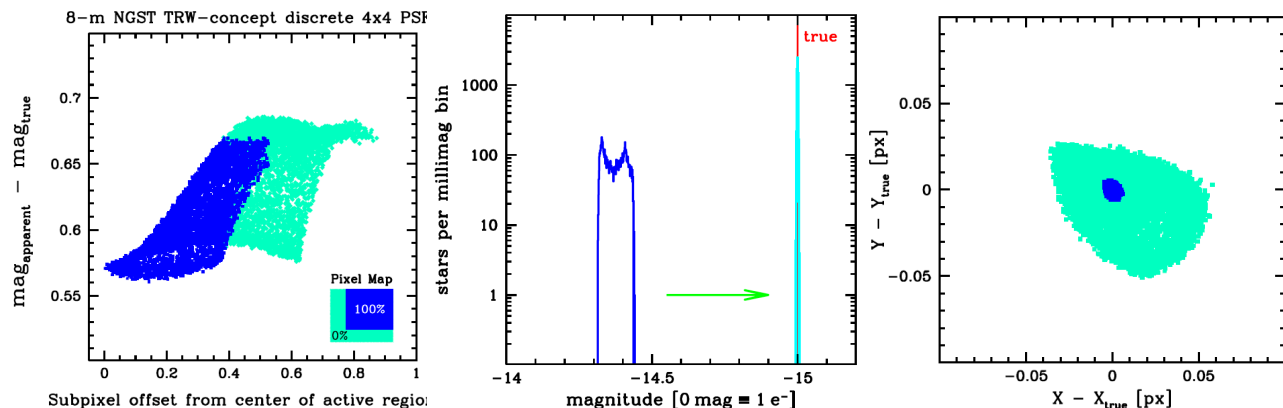


Figure 3. Results of the MPDX experiment with simulated NGST observations.

The optically inactive gate structures of the pixel cause the observed number of electrons in each stellar image to be significantly less than the number of photons which fell on the detector. *The total amount of loss was dependent on where the center of the star fell within the central pixel of the stellar image.* The left side of Fig. 3 shows that stars centered in the middle of the active area of a pixel suffered a $\sim 40\%$ loss ($\Delta m \approx 0.56$ mag) while those centered on gate structures lost up to 47% ($\Delta m \approx 0.69$ mag).⁶

The mean *apparent* (observed) stellar magnitude for these -15 mag stars was -14.3723 ± 0.0354 mag. The photometric performance model predicts an rms measurement error of 0.0015 mag for these bright stars. With an average loss of 44% and an rms measurement error that is *more than 23 times larger* than expected from photon statistics, *the observed stellar magnitudes were neither precise or accurate* (see the left histogram of the central graph in Fig. 3).

The mean *measured* stellar magnitude reported by MPDX was -14.9999 ± 0.0015 mag and the mean rms error estimated by the program was 0.001503 ± 0.000016 mag (see the right histogram of the central graph of Fig. 3). The photometric performance of the experimental version of MATPHOT is fully consistent with theoretical expectations — which were derived⁶ for an ideal detector with no intrapixel QE variation.

The experimental version of MATPHOT was able to do an excellent job in recovering the true stellar magnitude of the 10,000 -15 mag stars — despite being presented with a worst-case scenario of undersampled observations with an ugly PSF imaged on an ugly detector with a very large intrapixel QE variation.⁶

Non-uniform intrapixel response functions can also affect astrometric (position) measurements. Photons that are not converted to electrons can cause the apparent intensity weighted centroid of the PRF (i.e., the recorded stellar image) to be in a different location than the intensity weighted centroid of the PSF (i.e., the photon distribution function just above the detector). The right graph of Fig. 3 demonstrates this problem; the light grey (cyan) points show the large systematic astrometric errors of the *apparent* centroid (intensity weighted mean) of the stellar image; the black (blue) points show the small *random* astrometric errors of the MPDX measurements. In this particular experiment, the Fig. 3 indicates that the apparent position of the stellar image may in fact be several hundredths of a pixel off from the true location of the PSF — this is a very large systematic error considering that the expected position error from photon statistics is only 1.7 millipixels.

The experimental version of MATPHOT was able to do an excellent job in recovering the true stellar position of the 10,000 -15 mag stars — despite the fact that the apparent positions of Point Response Functions were corrupted by the inactive gate structures.

Excellent stellar photometry and astrometry is possible with ugly PSFs imaged onto ugly detectors as long as the image formation process within the detector is accurately modeled by the photometric reduction code.

6. SPITZER SPACE TELESCOPE'S INFRARED ARRAY CAMERA

The following is an extract from the IRAC Data Handbook:¹⁹

The flux density of a point source measured from IRAC images depends on the exact location where the peak of the Point Response Function (PRF) falls on a pixel. This effect is due to the variations in the quantum efficiency of a pixel, and combined with the undersampling of the PRF, it is most severe in channel 1. The correction can be as much as 4% peak to peak. The effect is graphically shown in Figure 5.1 where the normalized measured flux density (y-axis) is plotted against the distance of the source centroid from the center of a pixel. The correction for channel 1 can be calculated from

$$\text{Correction} = 1 + 0.0535 \times \left[\frac{1}{\sqrt{2\pi}} - p \right] \quad (5.14)$$

where p is the pixel phase ($p = \sqrt{(x - x_0)^2 + (y - y_0)^2}$), where x, y , is the centroid of the point source and x_0 and y_0 are the integer pixel numbers containing the source centroid. The correction was derived from photometry of a sample of stars, each star observed at many positions on the array. The “ratio” on the vertical axis in Figure 5.1 is the ratio of the measured flux density to the mean value for the star. To correct the flux of a point source, calculate the correction from Equation 5.14 and divide the source flux by that correction. Thus, the flux of sources well-centered in a pixel will be reduced by 2.1%. Pixel phase corrections for other channels, if necessary, and after they have been more accurately determined than currently, will be given in future Data Handbook versions.

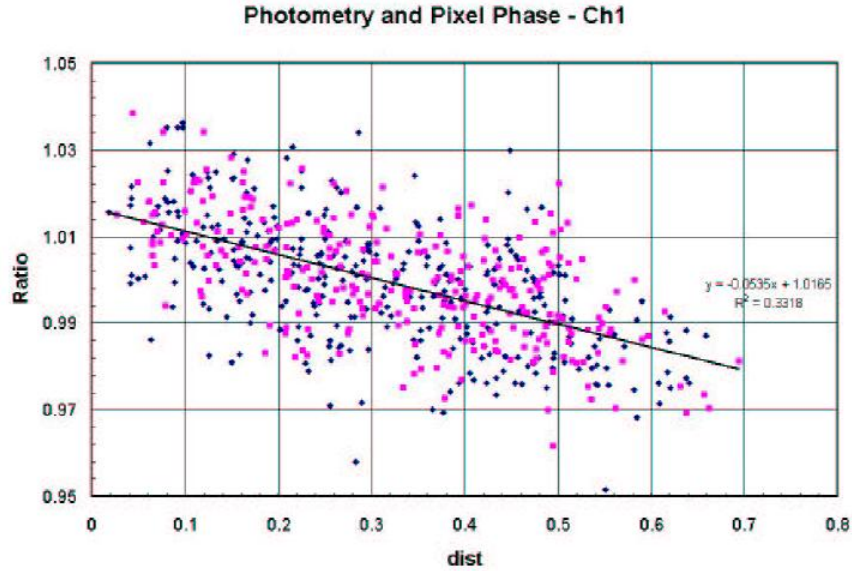


Figure 5.1: Dependence of point source photometry on the distance of the centroid of a point source from the nearest pixel center in channel 1. The ratio on the vertical axis is the measured flux density to the mean value for the star, and the quantity on the horizontal axis is the fractional distance of the centroid from the nearest pixel center.

Following discussions with *Spitzer Space Telescope's* Infrared Array Camera (IRAC) team members at the 207th meeting of the AAS in January 2006 in Washington, D.C., I have started working with various IRAC team members with the goal of determining if it might be possible to improve stellar photometry from IRAC's Channel 1 (3.6μ) by creating an experimental version of the existing MATPHOT code with an effective intrapixel quantum efficiency map for IRAC Ch1 hard-wired into the code.

Bill Hoffmann, an IRAC team member at the University of Arizona, has recently made the first estimate of the intrapixel QE variation across a single IRAC Channel 1 pixel:

$$\text{intrapix} = \begin{pmatrix} 0.813 & 0.875 & 0.875 & 0.875 & 0.813 \\ 0.875 & 1.000 & 1.000 & 1.000 & 0.875 \\ 0.875 & 1.000 & 1.000 & 1.000 & 0.875 \\ 0.875 & 1.000 & 1.000 & 1.000 & 0.875 \\ 0.813 & 0.875 & 0.875 & 0.875 & 0.813 \end{pmatrix}.$$

The mean conversion efficiency of this 5×5 convolution matrix is 91.01%. This is actually the *relative* intrapixel QE map since the central subpixels of this map were arbitrarily set to one; while the quantum efficiency of IRAC Channel 1 is high, the actual *absolute* values for the central subpixels are likely to be less than one. Full details about the derivation of this intrapixel quantum efficiency map may be found in Hoffmann's report *Intra-pixel Variation Effect on Aperture Photometry*.²⁰

Hoffmann²¹ has computed theoretical 5×5 supersampled versions of the IRAC Ch1 PSF across the camera's field-of-view. Fig. 4 shows the model PSF which was computed for the central region of the IRAC Ch1. The left side of Fig. 4 shows a linear stretch of the PSF and the right side shows a log stretch. Although the PSF appears to be reasonable in the linear stretch, which emphasizes the bright central core, the log stretch shows the numerous weak higher-spatial-frequency features of this very complicated PSF. IRAC Ch1 PSFs are significantly undersampled by the IRAC Ch1 camera;²² the mean effective background area⁶ (a.k.a. equivalent noise area⁵) is 7.0 pixels²³ as compared to the canonical value of 4π (~ 12.6 pixels) for a critically-sampled Gaussian PSF.

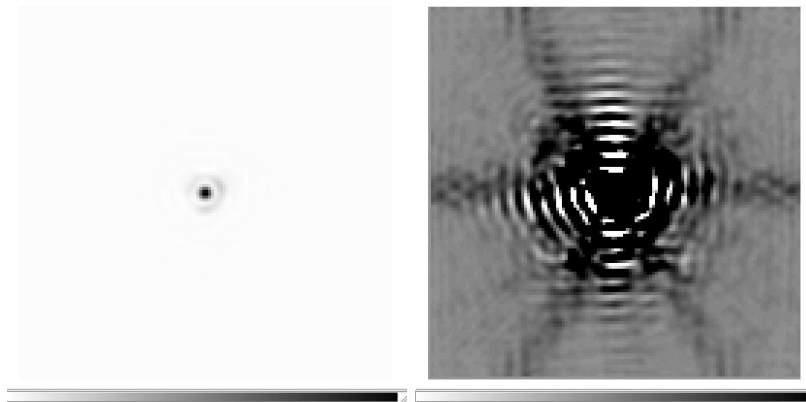


Figure 4. A theoretical 5×5 supersampled version of the IRAC Ch1 PSF.

Engineering decisions can significantly affect the science return of an instrument. The significant flux loss of IRAC Channel 1 is due to the combination of the non-negligible QE variation within a single pixel *and* the significant undersampling of the PSF by large (1.2 arcsec) pixels. The significant loss of flux in IRAC Ch1 could have been mitigated by simply oversampling the PSF. This capability was part of the initially proposed IRAC design which included both diffraction-limited and wide-field modes. The diffraction-limited mode was lost when the camera was simplified to include only the wide-field mode.

Image analysis software, which properly models the image formation process within the detector, has the *potential* of recovering the stellar flux lost by IRAC Ch1. Use of such software could thus enhance the science return from stellar (point source) observations which would appear, at first glance, to be limited to no better than 5% accuracy.

If an IRAC Ch1 observer follows the advice of the Infrared Array Camera Data Handbook¹⁹ and uses the suggested correction formula (given above) to compensate for the lost stellar flux, then there will remain a variation of about 2% which is due to the fact that much of the *vertical variation seen in Fig. 5.1 of the IRAC Data Handbook is systematic* rather than random; the true flux correction function is a complicated two-dimensional distribution that is not circularly symmetric.

In a collaborative research effort with Bill Glaccum (Spitzer Science Center), Bill Hoffmann, and other IRAC team members, I have succeeded in creating a new experimental version of MATPHOT, called MPDY, which uses Hoffmann's intrapixel QE variation map²⁰ and the theoretical 5×5 supersampled PSF shown in Fig. 4 to create and analyze realistic IRAC Ch1 simulated observations.

Ten thousand IRAC Ch1 observations of a single star on a flat background were simulated and analyzed with MPDY. Each stellar observation was simulated using the theoretical 5×5 supersampled IRAC Ch1 PSF shown in Fig. 4; a star with 10^5 electrons was located near the center of 60×60 pixels on a flat background of 100 electrons (e^-). The efficiency of the photon to electron conversion process is calculated using the Hoffmann intrapixel QE map given above. Realistically noisy data was created by adding photon noise and a readout noise level of $3 e^- \text{ pixel}^{-1}$. Fig. 5 shows some of the results of the MPDY analysis of these simulations.

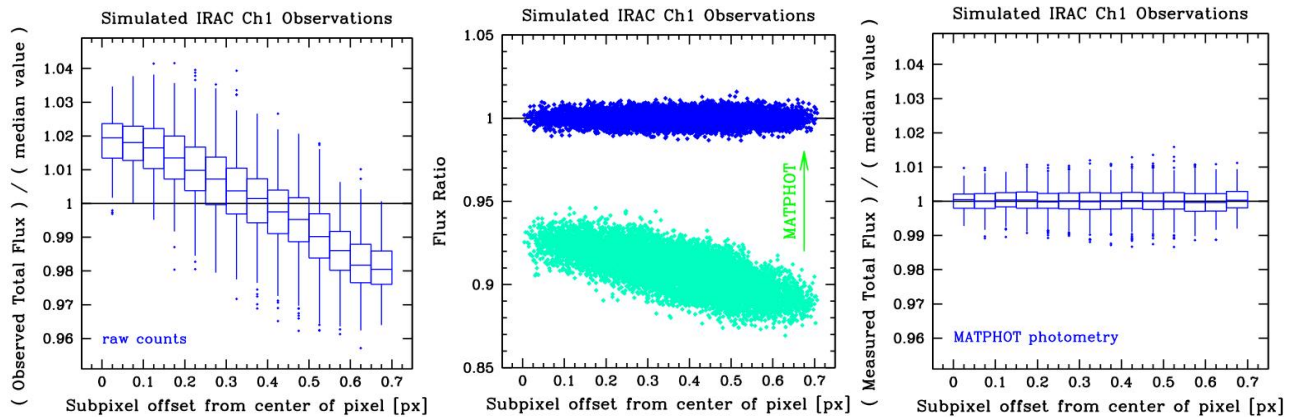


Figure 5. Results of the MPDY experiment with simulated IRAC Ch1 observations.

The horizontal axis of the left graph of Fig. 5 shows the subpixel offset (distance) the center of a star is from the middle of a pixel; stars centered near the middle of a pixel will have small offset values while stars located near the corner of a pixel will have offsets near 0.7 px. The vertical axis shows the *observed* (apparent) total flux divided by the *median observed* total flux value (90825.8 electrons, expected 100000) of all ten thousand stars. The median values of the box-and-whisker plots range from an excess flux of about 2% for stars centered near the center of a pixel to a flux deficit of about 2% for stars centered near the corner of a pixel. Note that this graph reproduces almost exactly the observed flux loss distribution seen in Fig. 5.1 of the IRAC Data Handbook.¹⁹

The vertical axis of the central graph of Fig. 5 shows the absolute flux ratio of the total fluxes divided by the true flux of 10^5 electrons. The light grey (cyan) points show the *observed* absolute flux ratios and the black (blue) points show the *measured* absolute flux ratios as reported by MPDY. Note that while the average stellar observation suffered an absolute flux loss of ~9%, stars centered near the middle of a pixel suffered, on average, an absolute flux loss of ~7% as compared to an absolute flux loss of ~11% for stars centered near a pixel corner. It is important to note that the vertical scatter seen in the observed flux ratios (absolute or relative) is not random but systematic; a simple radial correction function can only partially recover the lost flux. The measured absolute flux ratios are clustered around unity and are not a function of subpixel offset; the vertical scatter seen in the measured absolute flux ratios is random. By modeling the image formation process within the detector, MPDY was able to fully recover all of the stellar flux lost due to the non-uniform IRAC Ch1 intrapixel quantum efficiency variations.

The vertical axis of the right graph of Fig. 5 shows the *measured* total flux (as reported by MPDY) divided by the *median measured* total flux value (99972.3 electrons, expected 100000) of all ten thousand stars. This graph

shows that MPDY is able to recover the true stellar flux all the way down to the photon limit (photometric error of ~ 3.9 millimag).

The previous section showed how non-uniform intrapixel QE maps can potentially cause significant systematic astrometric (position) errors for bright stars. Would we expect the IRAC Ch1 QE map to create systematic astrometric errors? Yes, indeed. If an intrapixel QE map is roughly circularly symmetric about the middle of a pixel (as is apparently the case for IRAC Ch1), then the centroid of an observed stellar image (i.e., the PRF) *which is centered in the middle of a pixel* will be approximately at the same position as the centroid of the PSF. However, if there is significant flux loss near the edges or corner of a pixel (as is apparently the case for IRAC Ch1), then the *centroid of a PRF which is centered near a pixel corner will most likely not be the same as the centroid of the PSF* — and the difference will be a systematic error rather than a random error.

The major component of the systematic astrometric error is the undersampling of the PSF by IRAC Ch1. The intrapixel QE variation in the detector just makes the matter a little worse. Naively doing centroiding on the recorded undersampled stellar image may lead to astrometry which has dubious value. However, photometric reduction codes that model the image formation process within the detector can fully recover the true positions of the stars with precision described by the Cramér-Rao Lower Bound. While some undersampling can be tolerated without too much loss of astrometric precision, one should remember that moderation is a virtue. If the undersampling becomes severe enough that almost all of the light from a star falls within a single pixel, then the astrometric precision is significantly diminished.⁹

The MPDY experiment has been based on simulated IRAC Ch1 observations. So how well does MPDY work with real IRAC Ch1 observations? Hoffmann's IRAC Ch1 intrapixel QE map was based on Campaign Q focus observations²⁴ taken about 40 days after the launch of the *Spitzer Space Telescope*. The next obvious step in this research effort would be to analyze Campaign R data (taken 4 days later) with MPDY and determine just how well this theoretical approach works with real stellar near-infrared observations.

Mitigating the impact of flux loss problems seen in state-of-the-art NASA-grade infrared detectors is still in its early days. Hoffmann's IRAC Ch1 intrapixel QE map is the first attempt by the IRAC team to quantify this effect. Derivation of the intrapixel QE map is an *iterative process* due to the apparent centroid shifting caused by the non-uniform QE variation across a pixel; given an initial estimate of the intrapixel QE map, better positions of the input stellar images can then be determined, which, in turn, enables a better measurement of the intrapixel QE map to be made. Is a 5×5 map sufficiently fine enough to capture most of the PRF variations seen with IRAC Ch1? Would a 15×15 map be better or would that be overkill?

Much more work remains to be done. However, the possibility of significantly improving the precision and accuracy of space-based near-infrared stellar photometry and astrometry appears to be excellent. Ground-based infrared stellar photometry can typically achieve 10% accuracy and 5% accuracy under excellent conditions; the *Spitzer Space Telescope* is currently achieving only 5% photometry despite the fact that it is a cold stable observing platform in deep space. A significant improvement to 2-3% photometric accuracy might be possible with image analysis software that models the image formation process within the detector. A stretch goal of 1% photometric accuracy may even be achievable with *existing* space-based cameras using state-of-the-art infrared array detectors — if onboard cameras are electronically quiet and stable enough.

7. CONCLUSION

NASA and ESA astrophysical mission designers have a penchant to approve of optical designs that are under-sampled. Although excellent justifications can often be made for using complex optical designs that have ugly Point Spread Functions (e.g., reduced total mission cost) or for using detectors that are too big at a given wavelength (e.g., giving a wider field-of-view), the analysis of resultant image data from these designs is frequently problematical. Reliance upon traditional ground-based image analysis codes may preclude the use of innovative space-based optical designs if such designs are rejected during the design review process for the very practical reason that there is no proven way to accurately analyze the resultant image data.

The better a telescope and its instrumentation are characterized, the better one can extract the full scientific potential out of the telescope/instrument combination. Enhancing the scientific return of NASA's existing Great Observatories does not come without a real cost; better characterization of space-based instrumentation may

very likely require the development of new onboard calibration procedures. Some enhancements may be easy to achieve if the time spent doing the new calibrations can be folded into existing instrument calibration schedules. Other enhancements may simply not be practical – at this time – because current instruments may have electronic designs that are not quiet or stable enough to realize the enhancement. By learning from the good and bad engineering decisions that were made for existing astrophysical missions, we can enhance the scientific return of future astrophysical missions while possibly lowering total mission costs.

I hope that I have demonstrated that innovative image analysis software has great potential to act as a technology driver for advancing the state-of-the-art in the design of space telescopes and space-based instrumentation.

ACKNOWLEDGMENTS

I wish to thank Bill Hoffmann, Bill Glaccum, and the rest of the IRAC team for their support of this research effort which would not have been possible without the generous access they provided to previously proprietary data and reports. This work has been supported by a grant from the National Aeronautics and Space Administration (NASA), Interagency Order No. NNG05EB61I, which was awarded by the Applied Information Systems Research (AISR) Program of NASA's Science Mission Directorate.

REFERENCES

1. Technology Readiness Level Descriptions: <http://nmp.jpl.nasa.gov/st8-lib/NMP-TRL-Descriptions.pdf> .
2. New Millenium Program website: <http://nmp.nasa.gov> .
3. I. R. King, "The profile of a star image," *PASP* **83**, pp. 199–201, 1971.
4. J. Biretta, et al., *WFPC2 Instrument Handbook (Version 6.0)*, STScI, Baltimore, 2001.
5. I. R. King, "Accuracy of measurement of star images on a pixel array," *PASP* **95**, pp. 163–168, 1983.
6. K. J. Mighell, "Stellar photometry and astrometry with discrete point spread functions," *MNRAS* **362**, pp. 861–878, 2005.
7. M. J. Irwin, "Automatic analysis of crowded fields," *MNRAS* **214**, pp. 575–604, 1985.
8. N. Pogson, "Magnitudes of thirty-six of the minor planets for the first day of each month of the year 1857," *MNRAS* **17**, pp. 12–15, 1856.
9. K. A. Winick, "Cramér-Rao lower bounds on the performance of charge-coupled-device optical position estimator," *JOSA A* **3**, pp. 1809–1815, 1986.
10. MATPHOT web site: <http://www.noao.edu/staff/mighell/matphot> .
11. K. J. Mighell, "Algorithms for CCD stellar photometry," in *Astronomical Data Analysis Software and Systems VIII*, D. M. Mehringer, R. L. Plante, and D. A. Roberts, eds., *ASP Conference Series* **172**, pp. 317–328, 1999.
12. K. J. Mighell, "The MATPHOT algorithm for digital point spread function CCD stellar photometry," in *Astronomical Data Analysis II*, J.-L. Starck and F. D. Murtagh, eds., *Proc. SPIE* **4847**, pp. 207–216, 2002.
13. FITS Support Office web site: <http://fits.gsfc.nasa.gov> .
14. K. J. Mighell, "Accurate stellar photometry in crowded fields," *MNRAS* **238**, pp. 807–833, 1989.
15. K. Levenberg, "A method for the solution of certain problems in least squares," *Quarterly of Applied Mathematics* **2**, pp. 164–168, 1944.
16. D. Marquardt, "An algorithm for least-squares estimation of nonlinear parameters," *SIAM Journal of Applied Mathematics* **11**, pp. 431–441, 1963.
17. T. R. Lauer, "The photometry of undersampled point-spread functions," *PASP* **111**, pp. 1434–1443, 1999.
18. R. N. Hook and A. S. Fruchter, "Dithering, sampling and image reconstruction," in *Astronomical Data Analysis Software and Systems IX*, N. Manset, C. Veillet, and D. Crabtree, eds., *ASP Conference Series* **216**, pp. 521–530, 2000.
19. W. T. Reach, et al., *Infrared Array Camera Data Handbook (Version 3.0; January 20, 2006)*, [<http://ssc.spitzer.caltech.edu/irac/dh/iracdatahandbook3.0.pdf>], 2006.
20. B. Hoffmann, "Intra-pixel variation effect on aperture photometry," IRAC/TMo5-028 (Simfit Report 59; Version 2: December 10, 2005), 2005.

21. B. Hoffmann, "25 position model pixel response functions (prf) description and quality," IRAC/TMo5-014 (Simfit Report 52 Final), 2005.
22. R. D. Gehrz, et al., "The state of the focus and image quality of the Spitzer Space Telescope as measured in orbit," in *Optical, Infrared, and Millimeter Space Telescopes*, J. Mather, ed., *Proc. SPIE* **5487**, pp. 166–176, 2004.
23. G. G. Fazio, et al., "The Infrared Array Camera (IRAC) for the Spitzer Space Telescope," *APJS* **154**, pp. 10–17, Sept. 2004.
24. W. F. Hoffmann, et al., "Determination of Spitzer Space Telescope focus from irac images without a focus slew," in *Optical, Infrared, and Millimeter Space Telescopes*, J. Mather, ed., *Proc. SPIE* **5487**, pp. 186–2000, 2004.

Analysis of K-band Imaging of the Wide Binary System σ CrB with the Lick Observatory NGS AO System

Kenneth J. Mighell^a, Julian C. Christou^b, Jack D. Drummond^c

^aNational Optical Astronomy Observatory, 950 N. Cherry Ave., Tucson, AZ 85719, U.S.A.;

^bCenter for Adaptive Optics, University of California, 1156 High St., Santa Cruz, CA 95064, U.S.A.;

^cStarfire Optical Range, Directed Energy Directorate, Air Force Research Laboratory, Kirtland AFB, NM 87117, U.S.A.

ABSTRACT

We present astronomical results from K-band adaptive optics (AO) observations of the wide binary system σ Corona Borealis with the Lick Observatory natural guide star adaptive optics system on 2004 August 27–29. Seeing conditions were excellent and the AO compensation was very good, with Strehl ratios reaching 50% at times. The stellar images were reduced using three different analysis techniques: (1) Parametric Blind Deconvolution, (2) Multi-Frame Blind Deconvolution, and (3) the MATPHOT stellar photometry code. The relative photometric and astrometric precision achievable with these three analysis methods are compared. Future directions that this research can go towards achieving the goal of routinely obtaining precise and accurate photometry and astrometry based on near-infrared AO observations are described.

Keywords: binaries, astrometry, photometry, adaptive optics techniques, infrared instrumentation

1. INTRODUCTION

Adaptive optics (AO) photometry and astrometry of binary stars is problematic.¹ Photometry from AO observations of binary stars can exhibit errors (variations) which are larger than expected from simple noise analysis.^{2,3} Anisoplanatism and scintillation¹ are contributing factors to this observed variation, but other sources of photometric error include calibration errors, such as residual flat-fielding errors, and instrumental/detector errors, such as the location of the sources on the detector⁴ or *intrapixel* quantum efficiency variation in state-of-the-art optical and near-infrared cameras.^{5,6}

Photometric reduction errors can also be significant source of variation in AO observations of binaries. The proper measurement of the background sky level is essential yet is frequently surprisingly difficult in many AO observations of multiple star systems. Ground-based non-AO imagers generally have Point Spread Functions (PSFs) which are characterized as having most of their power at low spatial frequencies due to the combination of atmospheric turbulence and dome seeing. Space-based PSFs frequently have significant amounts of power at higher spatial frequencies due to the lack of blurring caused by atmospheric turbulence. AO imagers generally produce PSFs with characteristics found in both uncorrected ground-based PSFs and space-based PSFs: low-spatial-frequency features (e.g., broad halos) are combined with high-spatial-frequency features (e.g., sharp central cores and rings of the Airy pattern). Although the human eye is drawn to the sharp core of the AO PSF, that core frequently contains only a small fraction of the total energy from a given star; very large photometric apertures are typically required in order to achieve even 90% of the encircled energy. If the determination of the background “sky” level is based on the analysis of values of pixels that are too close to the core of the AO PSF, then the total flux of the star can be significantly underestimated in a way that can lead to *systematic* rather than random photometric errors. The fact that atmospheric turbulence typically causes the PSF to vary from short exposure to short exposure just makes the precision analysis of AO binary star observations that much more challenging.

In this article, we present astronomical results from K-band AO observations of the wide binary system σ Corona Borealis (σ CrB) with the Lick Observatory natural guide star adaptive optics system. This astrometric calibrator was chosen because the large separation between the two components would help minimize the many measurement challenges facing AO observations of binary systems that were mentioned above. Section 2 describes these observations and their reductions using three different analysis techniques: (1) Parametric Blind Deconvolution, (2) Multi-Frame Blind Deconvolution, and (3) the MATPHOT stellar photometry code. The relative photometric and astrometric precision achievable with these three analysis methods are discussed and compared in Section 3. The article concludes in Section 4 with a discussion of the future directions that this research can go towards achieving the goal of routinely obtaining precise and accurate photometry and astrometry based on near-infrared AO observations.

2. OBSERVATIONS AND REDUCTIONS

Observations of the wide binary system σ CrB (a.k.a. WDS J16147+3352, ADS 9979 AB, STF 2032) were obtained at the Lick Observatory 3-m Shane Telescope using the natural guide star (NGS) adaptive optics system⁷ with the IRCAL infrared imager⁸ on the nights of 2004 August 27-29. These observations were obtained in the K-band with a Brackett- γ filter we label $K(Br\gamma)$ ($\lambda_0 = 2.167 \mu\text{m}$; $\delta\lambda = 0.020 \mu\text{m}$). The seeing conditions were very good during the observing run with coherence length, r_0 (550 nm) values ranging from 8-18cm. The AO performance is typically characterized by the Strehl ratio with perfect performance, i.e. no aberrations in the optical system, having a value of 100%. The measured K-band Strehl ratios for a number of point source stars throughout the run ranged from 30-60%; a detailed discussion of the Strehl ratio calculation is given in Section 4 of Ref. 4.

The nominal image scale for the IRCAL camera is $0.076'' \text{ pixel}^{-1}$ so that the K-band observations are critically sampled with a theoretical resolution (λ/D) of $0.149''$. Figure 1 shows a single frame K-band observation of σ CrB. The diffraction-limited cores are clearly visible as well as the residual halo structure, due to the uncompensated components of the wavefront. The effects of the spiders are also seen in the Point Spread Functions (PSFs). Fig. 1 shows the strong degree of similarity in the structure between the widely separated PSFs.

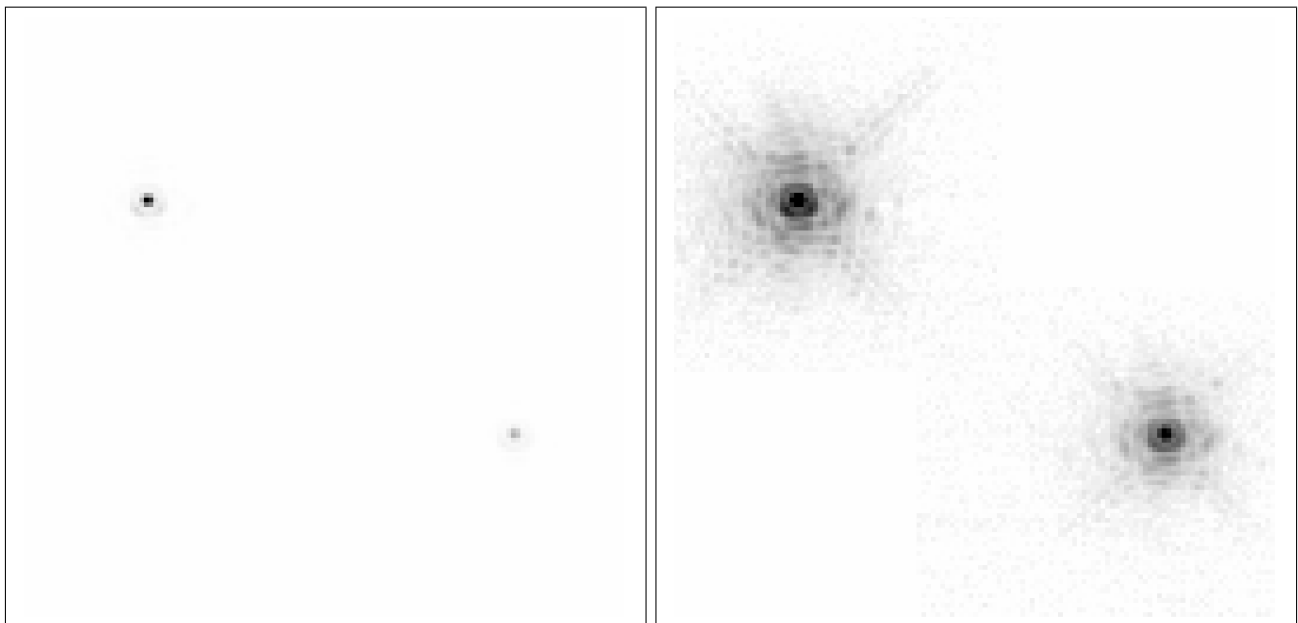


Figure 1. A portion of a single K-band observation of σ CrB obtained with the IRCAL infrared imager. The left side shows a linear stretch which emphasizes the bright central cores of the primary and secondary stars in this wide binary system. The right side shows a logarithmic stretch which emphasizes the faint halos as well as the effects of the spiders.

Each set of observations consisted of a series of short exposures (0.057-10 sec) which were initially preprocessed by sky-subtraction. The astrometry and photometry of the stars were obtained by three independent methods, Parametric Blind Deconvolution, Multi-frame Blind Deconvolution, and the MATPHOT⁶ stellar photometry code. The first two techniques have been previously successfully applied to binary star, multiple star and cluster adaptive optics observations;^{3,4,9} this is the first time the last technique has been applied to AO observations of binary stars.

Parametric Blind Deconvolution (PBD) models each of the PSFs in the image as a two-dimensional elliptical Lorentzian profile, which has been found to be an appropriate model for AO images. For this application, a Lorentzian profile was fit to each component in each of the separate frames in order to take into account any PSF variability across the field, i.e. anisoplanatism. A weighted mean, with the weights coming from the uncertainties of the fits, was computed for the separation angle (Sep), position angle (PA) and magnitude difference (Δm) for both stellar components. The PSFs in Figure 1 show departures from a Lorentzian model in that Airy rings are clearly visible. We compared the relative photometry and astrometry obtained from a Lorentzian fit to those obtained from a combined Lorentzian and Airy function fit to an observation of the multiple star system ι Cas (taken during this observation run) and found that the results did not change (within the dispersion of the measurements) which justified the use of the simpler parametric model for the analysis of the σ CrB observations.

Multi-frame Blind Deconvolution (MFBD) finds a common solution to a set of independent images of the same field assuming that the PSF varies from one frame to the next. The series of observations were broken into smaller subsets, typically four per set of observations, and a deconvolved image was computed with each component constrained to have a Gaussian shape at the end. The relative astrometry and photometry were computed by two-dimensional elliptical Gaussian fits to these deconvolved images. As for PBD, the weighted mean of the separation, position angle and magnitude difference were computed.

The MATPHOT⁶ stellar photometry code uses discrete (sampled) Point Spread Functions consisting of a numerical table represented by a matrix in the form of a FITS¹⁰ image. Discrete PSFs are shifted within an observational model using a 21-pixel-wide damped sinc function,

$$f^{\text{shifted}}(x_0) \equiv \sum_{i=-10}^{10} f(x_i) \frac{\sin(\pi(x_i - x_0))}{\pi(x_i - x_0)} \exp\left(-\left[\frac{x_i - x_0}{3.25}\right]^2\right), \quad (1)$$

and position partial derivatives are computed using a five-point numerical differentiation formula,

$$f'(x_i) \approx \frac{1}{12} [f(x_{i-2}) - 8f(x_{i-1}) + 8f(x_{i+1}) - f(x_{i+2})]. \quad (2)$$

Precise and accurate stellar photometry and astrometry are achieved with undersampled observations by using supersampled discrete PSFs that are sampled 2, 3, or more times more finely than the observational data. Although these numerical techniques are not mathematically perfect, they are sufficiently accurate for precision stellar photometry and astrometry due to photon noise which is present in all astronomical imaging observations.⁶ The current C-language implementation¹¹ of the MATPHOT algorithm is based on a robust implementation^{12,13} of the Levenberg¹⁴-Marquardt¹⁵ method of nonlinear least-squares minimization. Detailed analysis of simulated space-based CCD stellar observations demonstrate that millipixel relative astrometry and millimag photometric precision is achievable with complicated discrete PSFs.⁶

The MATPHOT stellar photometry code was developed for the analysis of space-based CCD cameras with complicated PSFs. We report the results obtained from the extension of the MATPHOT algorithm to ground-based AO PSFs.

The position and intensity of the primary and secondary stars were measured using the MATPHOT demonstrator program, MPD,^{6,11} with a discrete PSF derived from a normalized background-subtracted image of the primary star. As for PBD and MFBD, the weighted mean of the separation, position angle and magnitude difference were computed.

3. COMPARISON OF INDEPENDENT ANALYSIS TECHNIQUES

Christou and Drummond report⁴ that on 2004 August 28.90 the binary system σ CrB had the following parameters: a position angle of $237^\circ.5 \pm 0.1$, a large separation angle of 7.032 ± 0.008 arcsec, and $K(Br\gamma)$ magnitude difference of 1.01 ± 0.01 mag between the primary and secondary stars; these values were the unweighted mean and standard deviation of the PBD and MFBD results. The unweighted mean minimizes the effect of any systematic errors in one or the other of the two independent methods by favoring neither of them.

The left and central panels of Fig. 2 show, respectively, images of the primary and secondary stars taken from a single 3-second observation. The right panel of Fig. 2 shows the residuals in the region of the secondary star after the MATPHOT analysis has removed its best observational model (fit) from the image of the secondary star. The images in Fig. 2 are displayed with histogram equalization stretches in order to maximize the information content of each image. This enables us to see the strong degree of similarity in the fine structure details of the halos of the primary and secondary stars. Note the excellent removal by MATPHOT of the residual halo structure which is due to the uncompensated components of the wavefront. The right panel of Fig. 2 is graphical evidence that this observation occurred in the regime of partial-anisoplanatism where variation occurs mainly in the stellar cores.

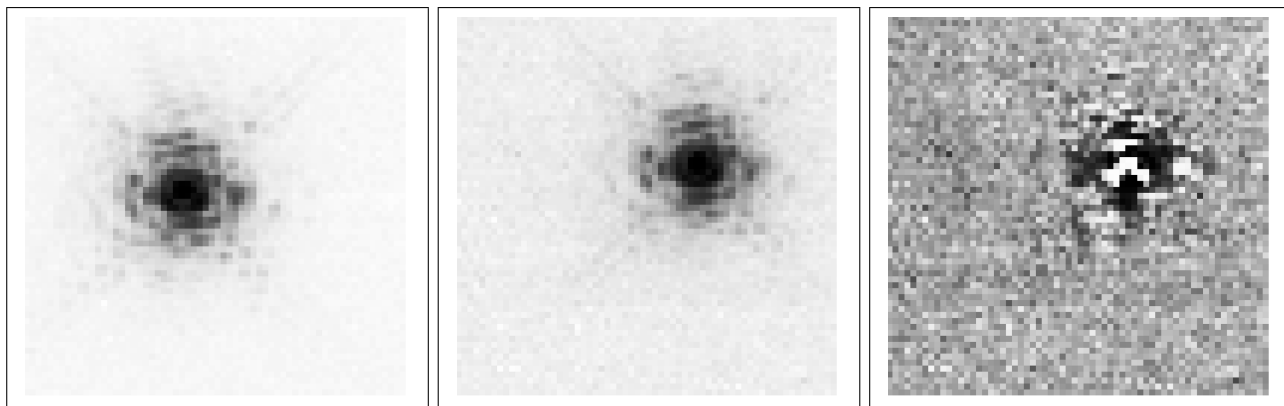


Figure 2. The primary (*left*) of σ CrB, the secondary (*middle*), and the residuals left after fitting PSF to the secondary. Histogram equalization stretches were used for all images; the relative dynamic ranges are, from left to right, 26.9 : 10.3 : 1 .

The results from the independent MATPHOT analysis are statistically identical to those reported for the previous PBD and MFBD analysis: PA= $237^\circ.5 \pm 0.1$, Sep= 7.015 ± 0.003 arcsec, and $\Delta m = 1.02 \pm 0.01$ mag. The fact that three very different analysis techniques all yield the same answers, within the statistical uncertainties, enhances our confidence in these results.

Our rms errors of the measured separation angle between the primary and secondary stars of σ CrB in individual observations (typically 2–3 mas) is very small when compared to the nominal IRCAL pixel size of 76 mas or the diffraction spot size (λ/D) of 149 mas. This precision in the measurement of the separation angle of a wide binary system has revealed a residual non-linearity in the spatial calibration (i.e., pincushion aberration) of the IRCAL infrared imager which, although it is smaller than the diffraction spot size, is still quite significant because it can cause systematic astrometric errors if its existence is not recognized.⁴

4. FUTURE DIRECTIONS

While the results of this study are quite encouraging for the future prospects for precision stellar photometry and astrometry using near-infrared detectors on adaptive optics systems, much work remains to be done before 1% photometry and milliarcsec relative astrometry are routinely achieved. Working with these observations has given us some insight on possible ways to improve ground-based near-infrared adaptive optics.

Ground-based observers using state-of-the-art infrared AO cameras at premier observing sites are now able to achieve milliarcsec spatial resolutions with near-diffraction-limited optics. For example, our natural guide star

AO observations with the IRCAL infrared imager yielded astrometric measurements with an angular resolution of just 2% of the diffraction spot size of a 3-m telescope (149 mas) and less than 5% the size of a small (76 mas) AO camera pixel. The fact that three independent AO stellar image analysis techniques are precise enough to reveal the existence of calibration errors in a state-of-the-art AO camera reveals the need for better (more accurate) plate scale calibrations for the detectors placed behind AO systems — if the full potential for relative astrometry with near-infrared AO stellar observations is to be reached. Better calibrations will require better astrometric calibrators, the creation of which will require the allocation of many observing nights with excellent seeing conditions on medium-to-large telescopes.

Searching for commonalities in different PSFs obtained with the same AO camera system on nights of similar excellent seeing conditions may now be feasible using image analysis tools like the MATPHOT stellar photometry code. Such a calibration effort may reveal an underlying non-negligible telescope-camera footprint on the PSF which is either stable on a nightly basis or varies slowly in a predictable manner possibly as a function of temperature. That knowledge could be combined with modeling of the atmospheric turbulence above the telescope and of the AO system itself to improve our ability to produce real-time predictions of the AO system PSF from real-time engineering information about the telescope and AO system — possibly including state information of individual actuators in the deformable mirror(s) within the optical path.

Having investigated the current limits of relative AO photometry and astrometry with a wide binary system, the next step is to see if the same precision levels can be achieved in studies of close binaries with overlapping PSFs and ultimately in very crowded stellar fields like that found near the Galactic center. While this investigation used a “simple” PSF, the MATPHOT algorithm was designed to handle complicated PSFs from space-based segmented telescopes (e.g., the *James Webb Space Telescope*); it would be very interesting to determine if these techniques will work as well with complicated PSFs from state-of-the-art laser guide star AO observations like those produced by the LGSAO system of the Keck II 10-m telescope (see Fig. 1 of Ref. 16).

Finally, the process of doing MATPHOT analysis on these observations has provided insights towards ways to improve the MATPHOT stellar photometry code so that it is more flexible, robust and easier to use. For example, the shift from optical to the near infrared has revealed the need to give the MATPHOT code the ability to use “error maps” associated with the observational data. Optical CCD stellar observations typically can be characterized with a simple noise model based on photon statistics (Poisson distributions) and shot noise (Gaussian distributions), while near-infrared stellar AO observations usually have their backgrounds subtracted — which can make it very difficult, if not impossible, to create a reliable noise model for a near-infrared observation based on assumptions which were valid for optical CCD observations. Giving MATPHOT the ability to use “error maps” — generally produced by calibration pipelines — not only relieves the program from the burden of having to produce a noise model of the observation, but it also makes the program more flexible in its ability to work with optical and infrared observations.

ACKNOWLEDGMENTS

We would like to thank the staff of Lick Observatory, in particular Elinor Gates, the AO Support Scientist for her valuable assistance with the AO system, and also many useful discussions with Donald Gavel. This work has been supported by a grant from the National Aeronautics and Space Administration (NASA), Interagency Order No. NNG05EB61I, which was awarded by the Applied Information Systems Research (AISR) Program of NASA’s Science Mission Directorate and by the National Science Foundation Science and Technology Center for Adaptive Optics, managed by the University of California at Santa Cruz under cooperative agreement No. AST - 9876783.

REFERENCES

1. L. C. Roberts, et al., “Adaptive optics photometry and astrometry of binary stars,” *AJ* **130**, pp. 2262–2271, 2005.
2. T. A. ten Brummelaar, et al., “Scientific results using the Mount Wilson Institute adaptive optics system,” in *Adaptive Optical System Technologies*, D. Bonaccini and R. K. Tyson, eds., *Proc. SPIE* **3353**, pp. 391–397, 1998.

3. D. Barnaby, E. Spillar, J. C. Christou, and J. D. Drummond, "Measurements of binary stars with the Starfire Optical Range adaptive optics systems," *AJ* **119**, pp. 378–389, 2000.
4. J. C. Christou and J. D. Drummond, "Measurements of binary stars, including two new discoveries, with the Lick Observatory adaptive optics system," *AJ* (**in press**), 2006.
5. T. R. Lauer, "The photometry of undersampled point-spread functions," *PASP* **111**, pp. 1434–1443, 1999.
6. K. J. Mighell, "Stellar photometry and astrometry with discrete point spread functions," *MNRAS* **362**, pp. 861–878, 2005.
7. B. J. Bauman, et al., "New optical design of adaptive optics system at Lick Observatory," in *Adaptive Optics Systems and Technology*, R. K. Tyson and R. Q. Fugate, eds., *Proc. SPIE* **3762**, pp. 194–200, 1999.
8. J. P. Lloyd, et al., "IRCAL: the infrared camera for adaptive optics at Lick Observatory," in *Optical and IR Telescope Instrumentation and Detectors*, M. Iye and A. F. Moorwood, eds., *Proc. SPIE* **4008**, pp. 814–821, 2000.
9. J. D. Drummond, "Adaptive optics Lorentzian point spread function," in *Adaptive Optical System Technologies*, D. Bonaccini and R. K. Tyson, eds., *Proc. SPIE* **3353**, pp. 1030–1037, 1998.
10. FITS Support Office web site: <http://fits.gsfc.nasa.gov> .
11. MATPHOT web site: <http://www.noao.edu/staff/mighell/matphot> .
12. K. J. Mighell, "Accurate stellar photometry in crowded fields," *MNRAS* **238**, pp. 807–833, 1989.
13. K. J. Mighell, "Algorithms for CCD stellar photometry," in *Astronomical Data Analysis Software and Systems VIII*, D. M. Mehringer, R. L. Plante, and D. A. Roberts, eds., *ASP Conference Series* **172**, pp. 317–328, 1999.
14. K. Levenberg, "A method for the solution of certain problems in least squares," *Quarterly of Applied Mathematics* **2**, pp. 164–168, 1944.
15. D. Marquardt, "An algorithm for least-squares estimation of nonlinear parameters," *SIAM Journal of Applied Mathematics* **11**, pp. 431–441, 1963.
16. A. M. Ghez, et al., "The First Laser Guide Star Adaptive Optics Observations of the Galactic Center: Sgr A*'s Infrared Color and the Extended Red Emission in its Vicinity," *ApJ* **635**, pp. 1087–1094, 2005.

Strehl ratio and image sharpness for Adaptive Optics

Julian C. Christou^a, Kenneth J. Mighell^b and Russell B. Makidon^c

^a Center for Adaptive Optics, University of California, Santa Cruz, CA 95064, USA.

^b National Optical Astronomy Observatories, Tucson, AZ 85719, USA.

^c Space Telescope Science Institute, Baltimore, MD 21218, USA.

ABSTRACT

The performance of an adaptive optics system is typically given in terms of the Strehl ratio of a point spread function (PSF) measured in the focal plane of the system. The Strehl ratio measures the normalized peak intensity of the PSF compared to that of an ideal PSF, i.e. aberration-free, through the system. One advantage of this metric is that it has been shown to be proportional to the rms wavefront error via the Marechal approximation. Thus, Strehl ratio measurements are used to determine the performance of the system. Measurement of the Strehl ratio is frequently problematic in the presence of noise as can be the peak determination for critically sampled data. We have looked at alternative metrics, in particular the S_1 sharpness metric. This metric measures the compactness of the PSF by the normalized sum of the squared image intensity and therefore relates to the intensity variance of the image. Using simulated AO PSFs, we show that there is a unique relationship between S_1 and the Strehl ratio and we can therefore relate it back to the rms wavefront error.

Keywords: adaptive optics, system performance, Strehl ratio, Image Sharpness

1. INTRODUCTION

The performance of an Adaptive Optics (AO) system is generally given in terms of the Strehl ratio (S). This metric lies between zero and unity with the latter defining the ideal point spread function (PSF) obtained with aberration free optics for the system in question. Essentially, S is the measurement of the normalized peak in the image. Aberrations in the wavefront cause the image to be less peaked than in the ideal image, therefore reducing the value of S . Furthermore, the Strehl ratio relates to the rms wavefront error ϕ by means of the extended Marechal approximation¹,

$$S \approx e^{-\phi^2} \quad (1)$$

and can therefore be used to estimate the residual wavefront error for AO systems. However Strehl ratio computations can be problematic². This is due to a number of factors, most notably (i) finding the sub-pixel peak value in the measured PSF and (ii) accurate determination of the zero-mean background or bias in the image. For Nyquist-sampled data, the peak-pixel value depends very strongly upon the sub-pixel location of the peak and can vary by almost a factor of two depending on whether the peak is centered on a single pixel or at the corner of four pixels. The presence of the non-zero background or bias in the data further complicates the computation because of the photometric normalization required when comparing to the total energy in the aberration-free PSF.

In this report we compare the application of one of the image sharpness metrics originally proposed by Muller and Buffington³, namely the S_1 metric which is insensitive to the peak location.

2. IMAGE QUALITY METRICS

The Strehl ratio is defined as follows:

$$S = \frac{h_{pk}}{\sum_i h_i} \bigg/ \frac{p_{pk}}{\sum_i p_i} = \frac{h_{pk}}{p_{pk}} \quad (2)$$

where h is the measured PSF, p is the ideal PSF and the $_{pk}$ subscript represents the peak value. When both PSFs are normalized to the same volume, then the Strehl ratio is simply the ratio of the peak values. Computation of S is not necessarily trivial². Firstly, real data is discrete and the peak value is not always centered on a single pixel but usually at a sub-pixel location (see §4). Thus a valid interpolation procedure is needed to compute the peak value when its location is known. Secondly there is the computation of the ideal PSF. This can be either done analytically or numerically. For simple optics, the former is relatively straightforward making use of analytic descriptions of diffraction with circular apertures. For astronomical imaging especially, the optical path can be further complicated by the presence of spiders, which support the secondary, and by non-circular pupils such as the hexagonal segmented aperture of the Keck telescopes. For these applications, numerical wave-optics propagation is necessary. Furthermore, the effects of pixel-binning and bandwidth have also to be taken into account for accurate Strehl ratio determination.

Other techniques exist to calculate the image quality. These have been discussed in a seminal paper by Muller and Buffington³. Three such techniques have been previously applied to speckle imaging data for frame selection⁴ and these are discussed below.

The first is the S_3 sharpness parameter as defined by Muller and Buffington which is simply the ratio of the peak value in the image normalized by the total power of the image, i.e.

$$S_3 = \frac{h_{pk}}{\sum_i h_i} \quad (3)$$

and is directly proportional to the Strehl ratio.

The second is the S_1 sharpness parameter which is related to the variance of the intensity values of the image, i.e.

$$S_1 = \frac{\sum_i h_i^2}{(\sum_i h_i)^2} \quad (4)$$

The image intensity variance can be expressed as

$$\sigma_h^2 \approx \langle h^2 \rangle - \langle h \rangle^2 = \frac{\sum_i h_i^2}{N^2} - \left[\frac{\sum_i h_i}{N} \right]^2 \quad (5)$$

so that

$$S_1 = \frac{\sigma_h^2}{N^2 \langle h \rangle^2} + \frac{1}{N^2} = A \sigma_h^2 + B \quad (6)$$

The third parameter is a measure of the width of the image as defined by the first- and second-order image moments, i.e.

$$\sigma_w^2 = M_2 - M_1^2 \quad (7)$$

and the j^{th} moment is given as

$$M_j = \frac{\sum_i h_i r_i^j}{\sum_i h_i} \quad (8)$$

where r_i is the distance of the i^{th} pixel from the image center. For the analysis below it is convenient to have all three metrics to increase or decrease together such that the metrics are smaller for larger distributions and larger for smaller distributions, i.e. more pointed images. Thus the inverse of σ_w is computed.

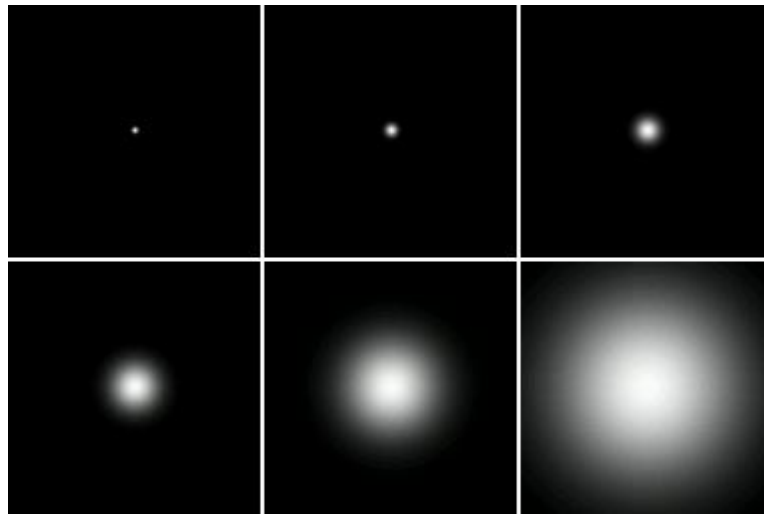


Fig. 1: Gaussians used to demonstrate the sensitivity of the different image quality measurements, S_1 , S_3 and σ_w .

In order to demonstrate the effectiveness of these parameters, they were applied to a set of Gaussians of different widths as shown in figure 1. The Gaussians were generated in a 256×256 pixel image and doubled in size successively from an initial Gaussian width of σ of 1 to 32. Figure 2 compares the input Gaussian width to the different image quality measurements. These results clearly demonstrate that all three measures are sensitive to the size of the Gaussian spot and readily distinguish relative changes in the compactness of the image.

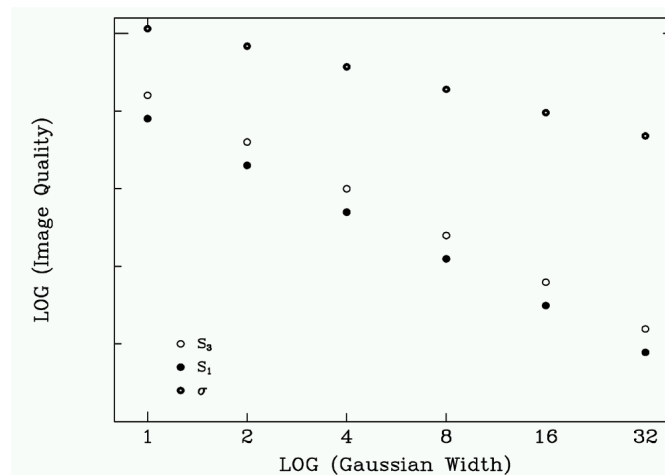


Fig. 2: Image quality measurements, S_1 , S_3 and σ_w , applied to the six Gaussians shown in Fig. 1.

Previous work⁴ has shown that these three metrics distinguished non uniformly illuminated “blobs”, i.e. uncompensated short exposure images - specklegrams - according to changes in the instantaneous seeing as measured by the Fried parameter r_o and were successfully used for frame selection.

3. SIMULATED ADAPTIVE OPTICS IMAGES

We generated a set of synthetic noise-free AO images following the approach used by Roberts et al. in a recent paper on Strehl ratio determination². Here, our simulations are characterized by the Palomar 5 m telescope entrance pupil size and geometry, namely a 5.08 m diameter aperture with an occulting secondary mirror of 1.83 m in diameter. We assumed a pixel scale of 50.04 pixels/m in the aperture, giving us 256 pixels across the clear aperture at the center of a 512 x 512 zero-filled array. We did not model the secondary mirror support structure ("spiders") as part of these simulations.

Our atmosphere was represented by a set of ten independent 512 x 512 Kolmogorov-spectrum phase screens with $D / r_0 = 15$ over the simulated aperture at a wavelength of $\lambda = 1.635\mu\text{m}$. Following the methods of Sivaramakrishnan et al.⁵, we Fourier-transform these input phase arrays and multiply them by a "parabolic" filter in spatial frequency space to mimic the action of AO. We reverse-transform the filtered arrays to obtain the AO-corrected wave fronts, and then create the complex phasor $\exp[i\phi(x,y)]$ describing the electric field corresponding to the AO-corrected phase $\phi(x,y)$. We then multiply these complex phasors by the array representing the telescope aperture, embed the filtered and masked array in the center of a 2048 x 2048 zero-filled array, and Fourier-transform the resultant array to obtain the image field. We square both the real and complex portions of the image field to produce our PSF. Our choice of final array size provides us with a sampling of $\lambda / 8D$ in the image plane.

Since the cut-off frequency of our AO filter cannot be higher than the spatial Nyquist frequency of the actuator spacing (as projected on to the primary mirror diameter), the number of actuators across the pupil determines the quality of our simulated AO compensation. Twelve different levels of AO correction were simulated by adjusting the number of actuators across the diameter of the telescope pupil (N_{act}), ranging from very poor ($S = \sim 5\%$) to very good ($S = 99\%$) wavefront compensation. Ten different wavefront realizations for each Strehl value were computed. The shift-and-add images of these ten frames are shown in Fig. 3 representing the mean tilt-free PSF for each of the twelve cases. Unlike the Gaussian cases illustrated in Fig. 1 the PSFs show different spatial frequency structure with a diffraction-limited core visible in all of them and the residual "seeing" halo shrinking considerably as the compensation improves.

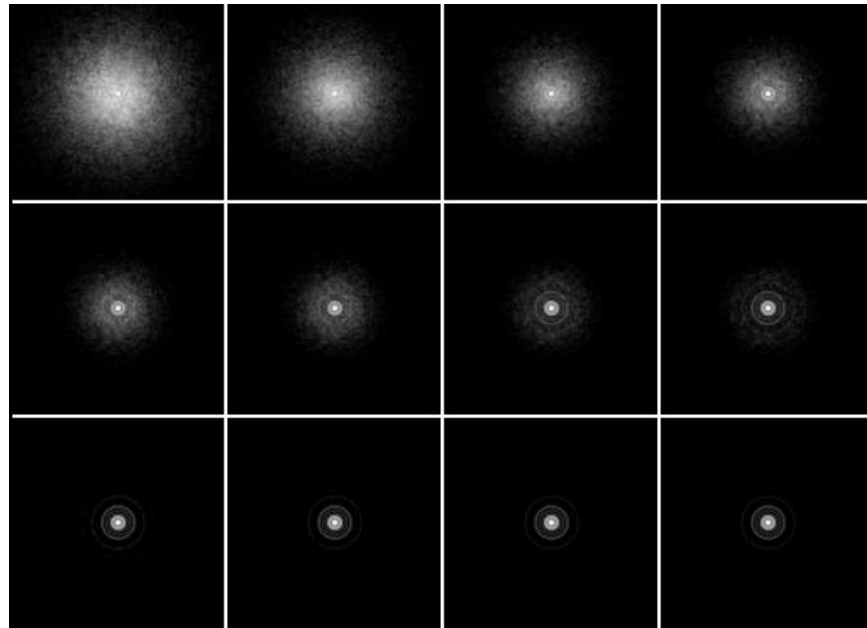


Fig. 3: Mean point spread functions for the twelve different levels of wavefront correction for the noise-free simulations (Logarithmic display)

4. IMAGE QUALITY METRICS APPLIED TO AO IMAGES

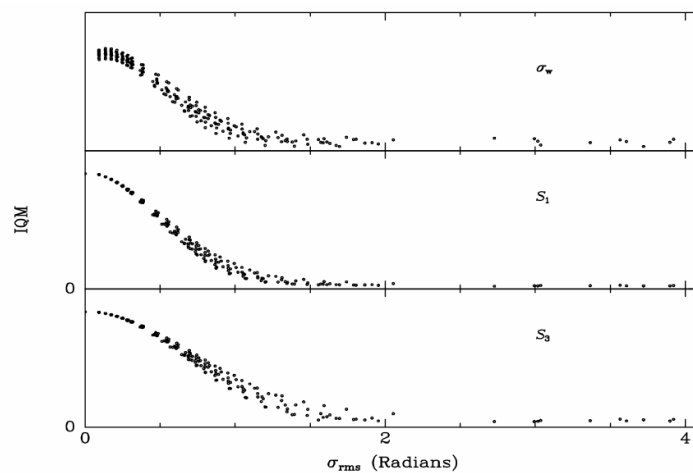


Fig. 4: Image quality metrics for the individual realizations for each of the different AO corrections.

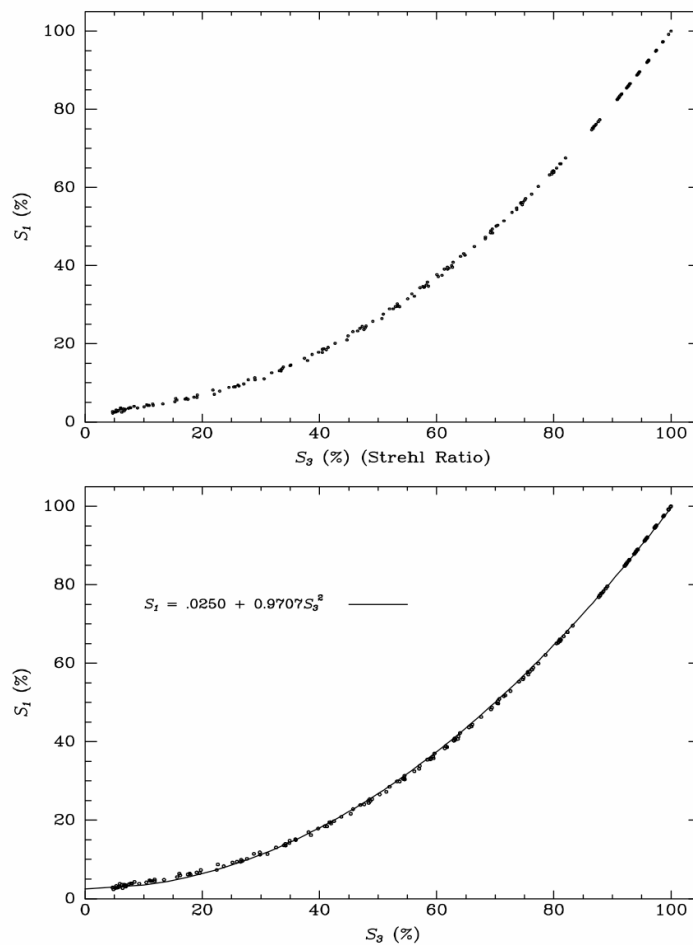


Fig. 5: Comparison of the normalized image sharpness metrics as shown in Fig. 4 for (top) the full sized image and (bottom) for the Nyquist sampled image which also shows the quadratic relationship between the two.

Fig. 4 shows the three image quality metrics for each of the 10 different realizations of the 12 different AO corrections using photometric aperture of $128 \lambda / D$. As can be seen, both S_1 and S_3 nicely track the variation in image quality. As the rms wavefront error decreases, the image quality as measured by these parameters improves and also shows less scatter. The image width also shows a similar trend with its inverse increasing as the compensation improves. However, this appears to be a rather insensitive measure in that the range of values is very small, less than 1% and this is in the presence of zero noise. Thus we limit further discussion of the image metrics to the two sharpness measures S_1 and S_3 . The relationship between these two metrics is shown in Fig. 5 which compares the two measures normalized to unity for the aberration-free case so that S_3 is now the Strehl ratio.

For a more realistic application the synthetic data was downsized to Nyquist sampling, i.e. 1 pixel = $\lambda / 2D$, and both sharpness parameters were then recomputed in the same physical aperture size.. There was no significant change in their normalized values from the original four times critically sampled generation. The least-squares fit of the two sharpness parameters was computed showing a quadratic relationship

$$S_1 = 0.0250 + 0.9707S_3^2 \quad (9)$$

between them which is not unexpected in that S_1 relates to the sum of the squared intensity in the image. This is also illustrated in Fig. 5. Thus $S_1 \propto \exp(-2\sigma^2)$.

It is important to note here that the image peak metric S_3 is sensitive to the effects of pixelization. By down-sampling, the peak is no longer located on a single pixel and an interpolation scheme is required to find the sub-pixel peak value. This can be done either by Fourier shifting⁶ or by using a damped sinc interpolator⁷. The former was used for the measurements shown in Fig. 5. The requirement for locating the sub-pixel peak value is illustrated in Fig. 6. Measuring the peak pixel value causes an underestimate of the metric which increases towards higher Strehl ratios as does the dispersion of the measurements. This is systematic behavior as more and more light is concentrated in the central pixel.

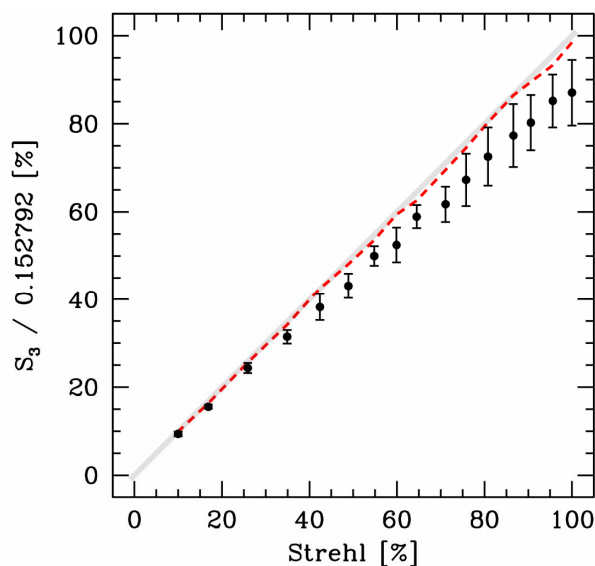


Fig. 6: The effects of pixelization of the measurement of the image peak, i.e. S_3 . The grey line shows the ideal case and the dashed line shows the maximum S_3 measurement for the data in the different AO compensation bins shown by their means and standard deviations.

4.1 The Effect of Additive Noise on Image Sharpness Metrics

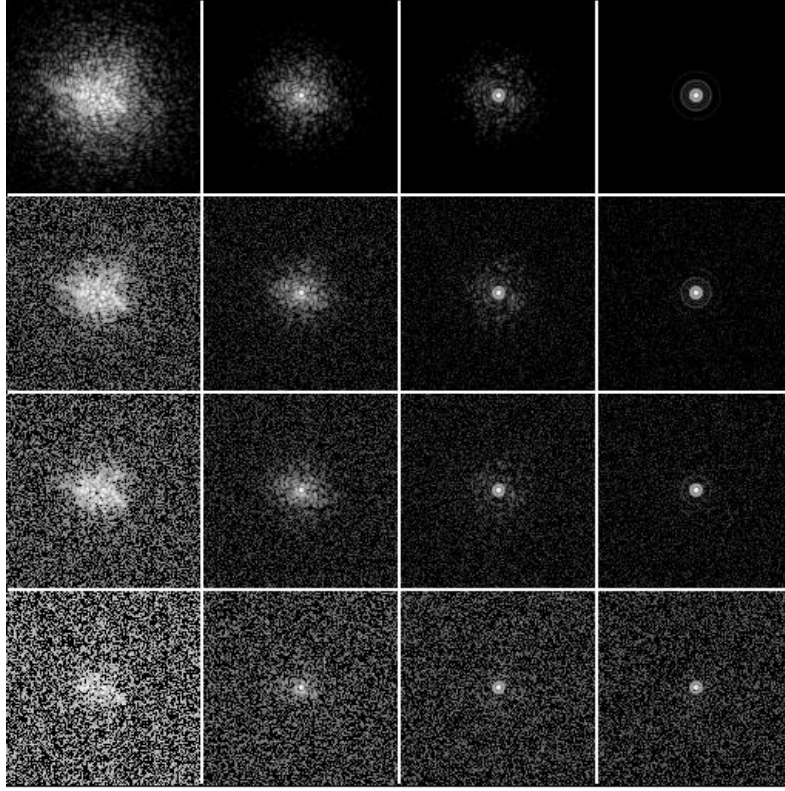


Fig. 7: Sample read-noise contaminated images for four of the different levels of AO compensation. Top-to-Bottom: noiseless, 41dB, 37dB and 31 dB. (All images displayed on a logarithmic scale from zero to maximum).

The previous section has clearly shown that either of the sharpness metrics can clearly distinguish the image quality of the AO compensated images as a function of the rms residual wavefront error for noiseless data. However, this is an unrealistic scenario and in this section we investigate the presence of additive read noise of these metrics simulating infrared AO observations. Zero-mean additive random noise simulating read noise was added to each of the different PSFs for four different signal-to-noise cases. The strength of the noise, measured as $-10\log_{10}\{P_n/P_s\}$, was 31dB, 37dB, 41dB and 47dB and its presence in the images is shown in Fig. 7.

The presence of noise affect both S_1 and S_3 sharpness measurements but in different ways. For S_3 which measures the image peak, a single realization of the noise on a single pixel, or the pixels surrounding the peak are affected. By comparison, the effect of noise on the measurement of S_1 is predictable. If the measured PSF is represented as

$$\tilde{h}_i = h_i + n_i \quad (10)$$

where n_i represents a single realization of zero-mean additive noise, then S_1 can be expanded as

$$\tilde{S}_1 = \frac{\sum_i \tilde{h}_i^2}{\left(\sum_i \tilde{h}_i\right)^2} = \frac{\sum_i (h_i + n_i)^2}{\left[\sum_i (h_i + n_i)\right]^2} = \frac{\sum_i h_i^2 + 2\sum_i h_i n_i + \sum_i n_i^2}{\left(\sum_i h_i\right)^2 + \left(\sum_i n_i\right)^2} \quad (11)$$

However as the noise is zero-mean and uncorrelated with the signal, then this expression simplifies to

$$\tilde{S}_1 = \frac{\sum_i h_i^2 + \sum_i n_i^2}{(\sum_i h_i)^2} = \frac{\sum_i h_i^2}{(\sum_i h_i)^2} + \frac{\sum_i n_i^2}{(\sum_i h_i)^2} = \frac{\sum_i h_i^2}{(\sum_i h_i)^2} + \frac{N\sigma_{\text{rms}}^2}{(\sum_i h_i)^2} = S_1 + \frac{N\sigma_{\text{rms}}^2}{(\sum_i h_i)^2} \quad (12)$$

where σ_{rms} is the rms of the additive noise and N the number of pixels used for the summation. Thus the metric is contaminated by a known bias term, assuming that the SNR is known.

Fig. 8 illustrates the effects of the additive noise in the determination of the two image sharpness metrics for the four different noise cases. These noise-contaminated parameters are plotted against the noise-free measurements showing the effect. For both S_1 and S_3 , it can be seen that as the noise increases the scatter in the correlation plots also increases. And for S_1 , the bias term given in (12) is clearly visible especially in the lowest SNR case. Fig. 9 shows the effect on the relationship between the two parameters due to the measurement noise. As seen in the Fig. 8, the three higher SNR cases appear to have little effect on either parameter. However, the lowest SNR case shows both a large scatter for the two measurements as well as the shift in S_1 due to the bias term as shown by the shifted quadratic fit.

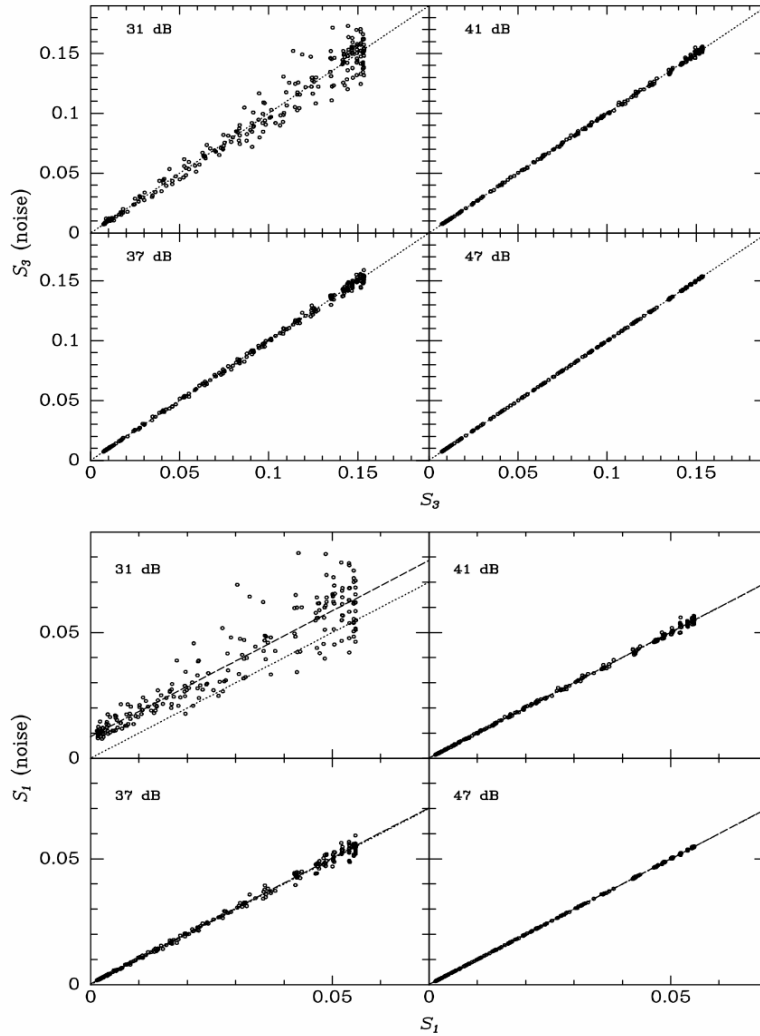


Fig. 8: The effect of additive zero-mean noise on the sharpness parameters for each of the synthetic images used for the noise-free measures. The dotted lines represent the noise-free correlation and the dashed lines for S_1 , the bias term in (12).

The effect of noise on the measured metrics is better investigated by looking at the fractional errors, $\Delta S_j = \{S_j - S_j'\} / S_j$, in their measurements when noise is present. This is illustrated in Figs. 10 and 11 for S_3 and S_1 respectively, which plots the fractional errors as a function of the rms residual wavefront error for the four different SNR cases studied. For S_3 it can be seen that the rms error increases as the SNR decreases as expected and for the three highest SNR cases, this error is less than 2% and approaches 10% for the lowest SNR case.

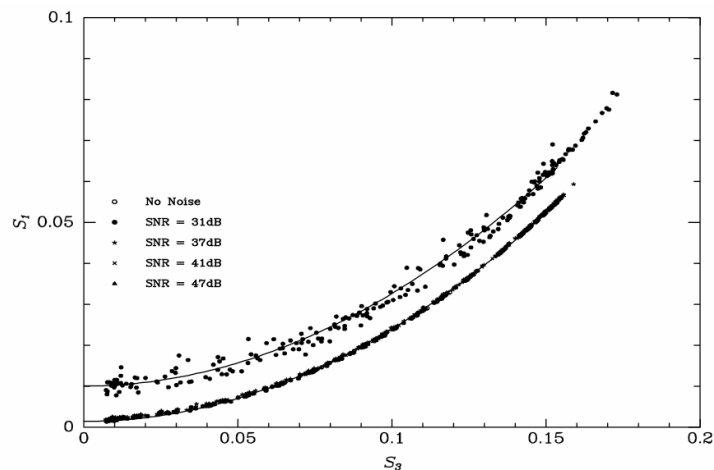


Fig. 9: The effect of additive zero-mean noise on the relationship between the two sharpness parameters. The solid lines represent the quadratic relationship between the two metrics for the noiseless and the lowest SNR cases.

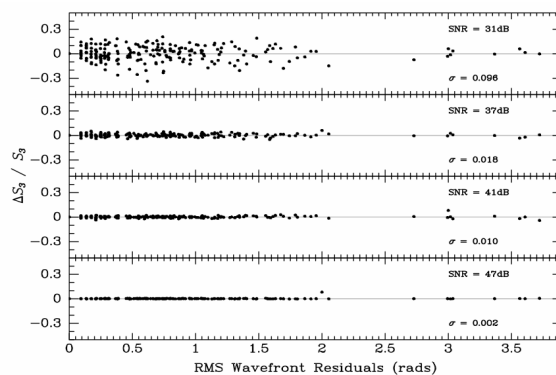


Fig. 10: Fractional errors on the estimate of the S_3 metric as a function of the rms wavefront error for the additive SNR conditions.

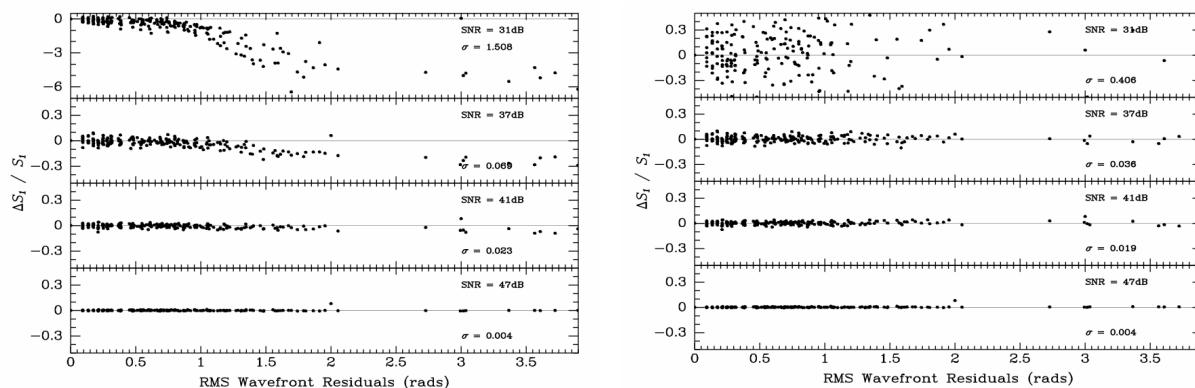


Fig. 11: Fractional errors on the estimate of the S_1 metric as a function of the rms wavefront error for the additive SNR conditions. Left: without noise bias subtraction; Right: with noise bias subtraction.

The fractional errors in S_1 depend very strongly upon the removal of the noise bias term in (12). Fig. 11 compares these fractional errors for the four different SNR cases with (bottom panel) and without (top panel) the noise bias removal. These plots further illustrate the need for this bias term to be calibrated. Once it is, comparison with the S_3 results, shown in Fig. 10, demonstrate that the performance of the two metrics is not too dissimilar. The rms fractional errors are given in Table 1 for the two metrics. This table shows that the fractional errors for S_1 are approximately twice those for S_3 except for the worst SNR case where it is approximately a factor of four greater. So what is the cause of the larger errors? Zero-mean additive noise was added to the images. However, each noise realization does not have an actual zero-mean value due to the finite number of pixels used to measure the image metric. For S_3 this shows up in the denominator only, whereas for S_1 this non-zero mean also contributes to the numerator. By comparison the numerator of S_3 is affected by a single noise term on the image peak.

Table 1: Fractional error in the image metric determination due to zero mean additive noise.

SNR (dB)	S_1	S_3
47	0.004	0.002
41	0.019	0.010
37	0.036	0.018
31	0.406	0.096

4.2 The Effect Signal Strength on Image Sharpness Determination.

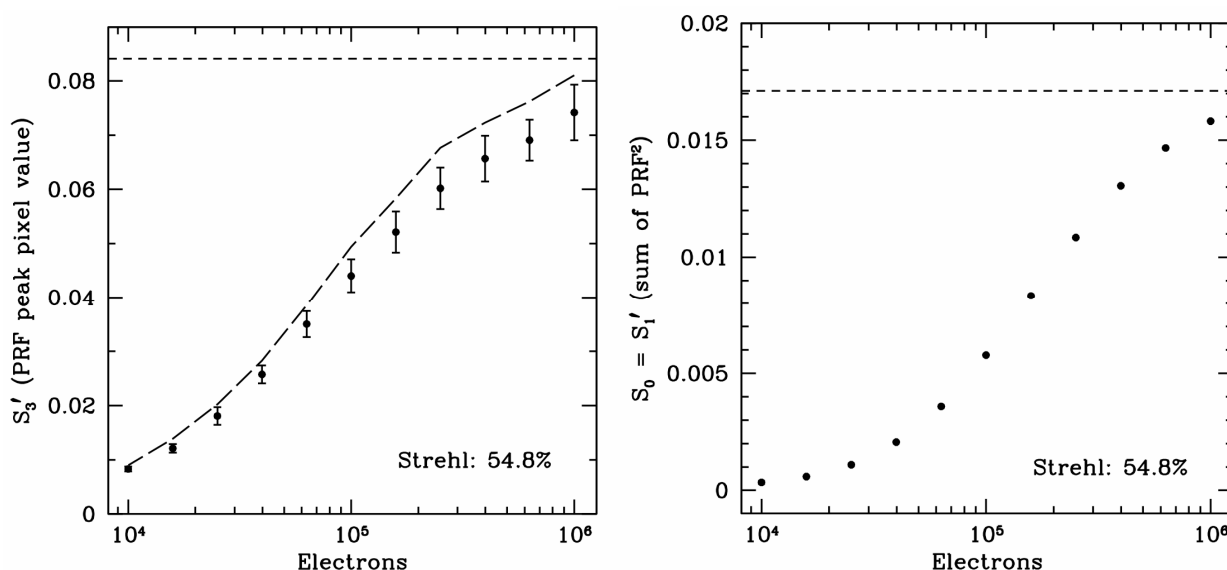


Fig. 12: The effect of signal strength on the computation of the two image sharpness parameters. These plots show the variation in measured image sharpness as a function of the number of electrons in the image. The short-dashed lines represent the perfect value of the sharpness metrics. The long-dashed line represents the maximum S_3 value. The metrics S'_3 and S'_1 represent the background subtracted estimates of the corresponding sharpness metrics.

Previously we looked at the effect of additive read noise on the measurement of the image sharpness metrics. This is important especially when dealing with infra-red observations. The MAPHOT package⁷ was used to generate twenty-five separate measurements of the same oversampled PSF at eleven different brightness levels. Each simulated observation had a background of 100 electrons and read noise of 3 electrons with a gain of unity, i.e. 1 electron per DN. The trend is obvious for both metrics. As the brightness of the source decreases, i.e. the number of electrons decreases, more and more positive background noise is diluting the source signal. This is the classic photometric problem of using too large a photometric aperture to measure the signal. However, if the aperture is reduced, then some source signal is omitted, i.e. outside of the aperture, so that normalization by the flux of an ideal PSF will generally result in an

overestimate of the Strehl ratio. It is interesting to note that for this scenario, even one million electrons is not sufficient to reach the ideal metric value falling short by $\sim 10\%$.

5. SUMMARY

In this report we have compared different approaches for measuring image quality of an Adaptive Optics system. We have demonstrated that over a broad range of correction with rms residual wavefronts corresponding to Strehl ratios of 5%-99%, that both major sharpness parameters initially suggested by Muller and Buffington³ behave well giving unique correlation in the metric as a function of the residual wavefront error. Furthermore, we have demonstrated that there is a quadratic functional relationship between the two such that $S_1 \propto S_3^2$ where S_3 is essentially the un-normalized Strehl ratio. Thus we can relate S_1 back to the rms wavefront residuals by means of the extended Marechal approximation.

We next investigated the presence of noise in the determination of these metrics. In the regime where additive background noise dominates such as for infrared observations, both metrics show a substantial increase in scatter as the noise increases. The S_1 metric also introduces a noise bias term even in the presence of zero-mean noise which is not the case for S_3 . However, given knowledge of the noise statistics, this bias term is predictable and can be removed from the metric estimate as demonstrated. The performance of both metrics for such noisy data was determined from the rms fractional error for the full range of compensation values for a given SNR case. It was found that S_3 had smaller errors and was less sensitive to the noise than the S_1 metric. In this analysis, it was assumed that the background was known absolutely to be zero but in working with real data this would not be the case, the classic photometric problem of accurately determining the background. The finite number of pixels used for both metrics affects S_1 doubly so that the non-zero mean thus produced will introduce extra error in the estimates especially as this is a metric which measures the square of the intensity. This represents a further study area for evaluating these metrics.

The second noise case we studied affected the signal strength, i.e. the number of photoelectrons in each image. It was found that this had a substantial effect on the value of both sharpness metrics measured. Under relatively realistic observing conditions with a million electrons in the signal, both metrics underestimated their noiseless values by $\sim 10\%$. This implies that for accurate determination of system performance where the metric is used to determine the rms residual wavefront error only bright sources should be used. This also implies that when comparing system performance over a number of nights, that stars of the same brightness should always be used. If bright sources are not available, then a correction factor will need to be applied. Future work includes investigation of what this correction factor would be for specific AO/camera systems using sophisticated computer end-to-end computer modeling. However for relative increase or decrease of system performance both would appear to be acceptable metrics. We recommend that stars with similar brightness and with similar exposure times should always be used where possible for evaluating performance changes over many different time scales.

Measuring Strehl ratio is problematic and for infrared AO observations even more so. Additional problems include accurate sky calibration especially so because the infrared sky can vary over time scales as short as single exposures which the precision with which the encircled energy fraction can be estimated.

ACKNOWLEDGEMENTS

This work has been supported by the National Science Foundation Science and Technology Center for Adaptive Optics, managed by the University of California at Santa Cruz under cooperative agreement No. AST-9876783. KJM was supported by a grant from the National Aeronautics and Space Administration (NASA), Interagency Order No. NNG05EB61I, which was awarded by the Applied Information Systems Research (AISR) Program of NASA's Science Mission Directorate. RBM is also a member of the Center for Adaptive Optics.

REFERENCES

1. J.W. Hardy, "Adaptive optics for astronomical telescopes", Oxford University Press, New York, (1998).
2. L.C. Roberts, M.D. Perrin, F. Marchis, et al, "Is that really your Strehl ratio?" Proc. SPIE, 5490, 504-515 (2004).
3. R.A. Muller, A. Buffington, "Real-time correction of atmospherically degraded telescope images through image sharpening", J. Opt. Soc. Am., 64,9, 1200-1211, (1974).
4. J.C. Christou, D.W. McCarthy, & M.L. Cobb, "Image selection and binning for improved atmospheric calibration of infrared speckle data", Astron. J., 94, 416-522, (1987).
5. A. Sivaramakrishnan, C.D. Koresko, R.B. Makidon, T. Berkefeld, and M.J. Kuchner, "Ground-based Coronagraphy with High-order Adaptive Optics," Astrophys. J., 552, 397-408, (2001).
6. S. Gladysz, J.C. Christou and M. Redfern, "Characterization of the Lick Observatory Point Spread Function", these proceedings (2006).
7. K.J. Mighell, "Stellar Photometry and Astrometry with Discrete Point Spread Functions", Mon. Not. R. Ast. Soc., 362, 861-878, (2005).

Improving the Precision of Near-Infrared Stellar Photometry by Modeling the Image Formation Process within a Lossy Detector¹

Kenneth Mighell

National Optical Astronomy Observatory, 950 N. Cherry Ave., Tucson, AZ 85719

ABSTRACT

Current infrared detector technology can produce imagers with non-uniform intrapixel response functions. Cameras based on such detectors can have large systematic errors in the measurement of the total stellar flux. Although this problem can be mitigated by oversampling the stellar image, many near infrared cameras are undersampled in order to achieve a large field of view. The combination of undersampling stellar images with non-uniform detectors is currently diminishing the science return of some infrared imagers onboard the *Hubble Space Telescope* and the *Spitzer Space Telescope*. Large intrapixel quantum efficiency variations can also cause significant systematic position measurement errors. Although the recorded flux and position of point sources is corrupted by using detectors with non-uniform intrapixel response functions, it is still possible to achieve excellent stellar photometry and astrometry — if the image formation process inside the detector is accurately modeled. A practical demonstration of how the precision and accuracy of near infrared stellar photometry can be significantly improved is provided by a detailed analysis of stellar observations obtained with Spitzer's Infrared Array Camera (IRAC) instrument.

1. PHOTOMETRY AND ASTROMETRY WITH DISCRETE POINT SPREAD FUNCTIONS

The MATPHOT algorithm for precise and accurate stellar photometry and astrometry with discrete (sampled) Point Spread Functions (PSFs) was described in detail by Mighell [1]. The current C-language [2] implementation of the MATPHOT algorithm works with user-provided discrete PSFs consisting of a numerical table represented by a matrix in the form of a FITS image [3]. Discrete PSFs are shifted within an observational model using a 21-pixel-wide damped sinc function [4] and position partial derivatives are computed using a five-point numerical differentiation formula [5]. Precise and accurate stellar photometry and astrometry are achieved with undersampled charge coupled device (CCD) observations by using supersampled discrete PSFs that are sampled 2, 3, or more times more finely than the observational data. Although these numerical techniques are not mathematically perfect, they are sufficiently accurate for precision stellar photometry and astrometry due to photon noise which is present in all astronomical imaging observations. The current photometric reduction code [6] is based on a robust implementation of the Levenberg-Marquardt method of nonlinear least-squares minimization [7–10]. Detailed analysis of simulated *Next Generation Space Telescope* observations demonstrate that millipixel relative astrometry and millimag photometric precision are achievable with complicated space-based discrete PSFs [1].

¹ This work is based on archival data obtained with the *Spitzer Space Telescope*, which is operated by the Jet Propulsion Laboratory, California Institute of Technology under a contract with NASA. Support for this work was provided by an award issued by JPL/Caltech.

2. OBSERVATIONS AND PHOTOMETRIC REDUCTIONS

Sixteen short (0.4 s) calibration observations of the K0 star PPM 9412 were obtained on 2003 October 8 UT with Channel 1 (3.6 μm) of the Infrared Array Camera (IRAC; [11]) onboard the *Spitzer Space Telescope* (see Table 1).

ID	RA_HMS	DEC_DMS	EXPTIME	DATE_OBS	DS_IDENT
1	17h06m11.6s	+73d40m11s	0.4	2003-10-08T11:55:51.356	ads/sa.spitzer#0006875392
2	17h06m11.1s	+73d40m11s	0.4	2003-10-08T12:08:56.748	ads/sa.spitzer#0006876672
3	17h06m10.8s	+73d40m10s	0.4	2003-10-08T12:22:01.538	ads/sa.spitzer#0006876928
4	17h06m10.6s	+73d40m09s	0.4	2003-10-08T12:35:06.524	ads/sa.spitzer#0006877184
5	17h06m11.3s	+73d40m12s	0.4	2003-10-08T12:48:11.510	ads/sa.spitzer#0006877440
6	17h06m10.9s	+73d40m12s	0.4	2003-10-08T13:01:16.496	ads/sa.spitzer#0006877696
7	17h06m10.5s	+73d40m11s	0.4	2003-10-08T13:14:21.489	ads/sa.spitzer#0006877952
8	17h06m10.2s	+73d40m11s	0.4	2003-10-08T13:27:26.471	ads/sa.spitzer#0006878208
9	17h06m11.0s	+73d40m14s	0.4	2003-10-08T13:40:31.472	ads/sa.spitzer#0006878464
10	17h06m10.7s	+73d40m13s	0.4	2003-10-08T13:53:36.446	ads/sa.spitzer#0006878720
11	17h06m10.5s	+73d40m13s	0.4	2003-10-08T14:06:41.436	ads/sa.spitzer#0006878976
12	17h06m10.0s	+73d40m12s	0.4	2003-10-08T14:19:46.422	ads/sa.spitzer#0006879232
13	17h06m11.0s	+73d40m15s	0.4	2003-10-08T14:32:51.423	ads/sa.spitzer#0006879488
14	17h06m10.5s	+73d40m15s	0.4	2003-10-08T15:06:39.788	ads/sa.spitzer#0006879744
15	17h06m10.3s	+73d40m14s	0.4	2003-10-08T15:19:44.785	ads/sa.spitzer#0006880000
16	17h06m10.0s	+73d40m13s	0.4	2003-10-08T15:32:49.763	ads/sa.spitzer#0006880256

Table 1. IRAC Ch1 Observations of PPM 9412

The IRAC basic calibrated data (BCD) images were retrieved from the Spitzer data archive. These observations were analyzed with the imexamine task of NOAO's Image Reduction and Analysis Facility (IRAF; [12–13]) package and a new experimental version of MATPHOT, called MPDZ, which uses the following relative intrapixel quantum efficiency (QE) variation map [14] for IRAC Channel 1 (Ch1),

$$\text{intrapix} = \begin{pmatrix} 0.813 & 0.875 & 0.875 & 0.875 & 0.813 \\ 0.875 & 1.000 & 1.000 & 1.000 & 0.875 \\ 0.875 & 1.000 & 1.000 & 1.000 & 0.875 \\ 0.875 & 1.000 & 1.000 & 1.000 & 0.875 \\ 0.813 & 0.875 & 0.875 & 0.875 & 0.813 \end{pmatrix},$$

and a theoretical IRAC Ch1 PSF [15] for the central region of IRAC Ch1 (see Fig. 1).

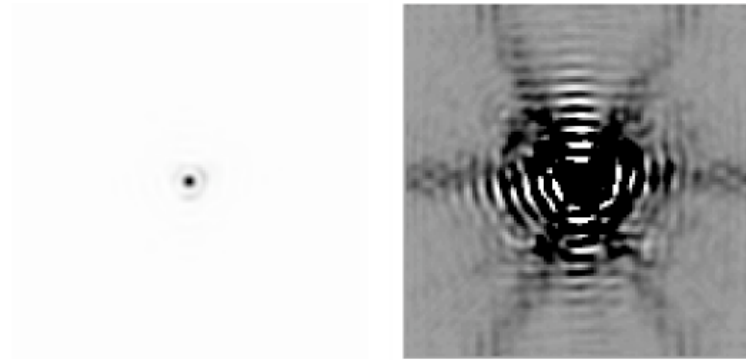


Fig. 1. A theoretical 5x5 supersampled version of the IRAC PSF for the central region of Ch1 [15]. The left side of 4 shows a linear stretch of the PSF and the right side shows a log stretch. Although the PSF appears to be reasonable in the linear stretch, which emphasizes the bright central core, the log stretch shows the numerous weak higher-spatial-frequency features of this very complicated PSF. IRAC Ch1 PSFs are significantly undersampled by the IRAC Ch1 camera [11].

3. SQUARE APERTURE PHOTOMETRY

Square aperture photometry with a 21x21 pixel box centered on the star was done using the interactive “m” keyboard command of IRAF’s imexamine task. Fig. 2 shows a 5.6% peak-to-peak spread in these square aperture flux measurements.

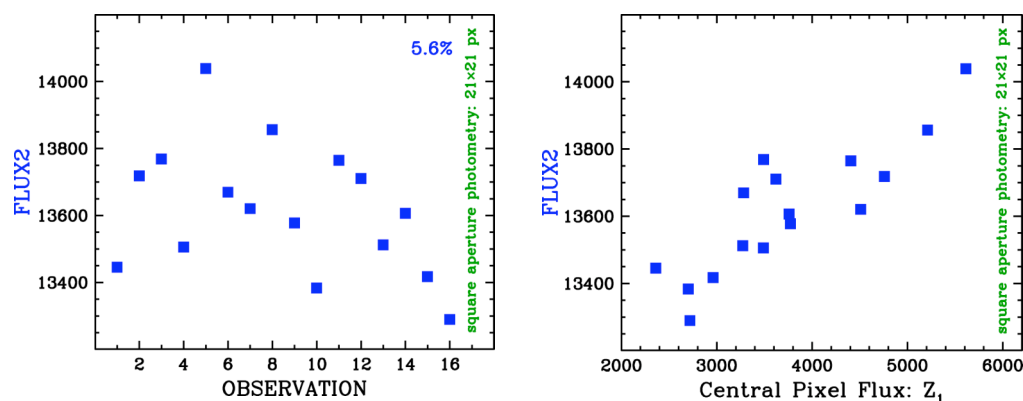


Fig. 2. Square aperture photometry (21x21 pixels)

The variation in flux seen in Fig. 2 is not completely random. The right graph of Fig. 2 shows that the total stellar flux is correlated with the amount of flux found in the central pixel. Examination of the individual observations reveal that the observations with the most stellar flux have stellar images that are centered in the middle of a pixel while those observations with the least stellar flux are centered on a pixel corner. This same effect is seen in Fig. 3 which is taken from the IRAC Data Handbook [16].

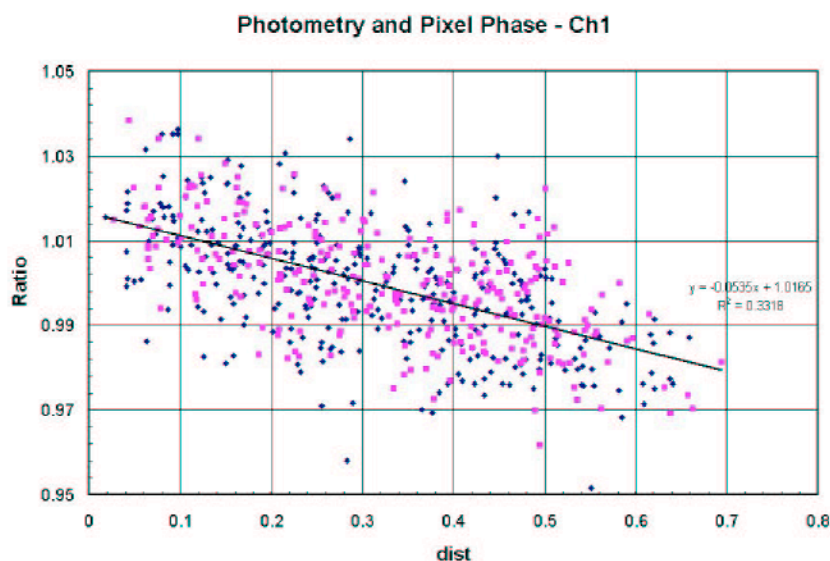


Fig. 3. Normalized measured flux density (y-axis) is plotted against the distance of the source centroid from the center of a pixel (source: Fig. 5.1 of the IRAC Data Handbook [16]).

The flux density of a point source measured from IRAC images depends on the exact location where the peak of the stellar image (the Point Response Function) falls within the central pixel of the stellar image. This effect is due to the variations in the quantum efficiency of a pixel, and combined with the undersampling of the PRF, it is most severe in Channel 1 [16]. The correction can be as much as 4% peak to peak.

4. CIRCULAR APERTURE PHOTOMETRY

Circular aperture photometry centered on the star with a radius of 10 pixels was done using the interactive “a” keyboard command of IRAF’s imexamine task. Fig. 4 shows a 5.3% peak-to-peak spread in the raw circular aperture flux measurements (open circles). Applying the recommended Ch1 flux correction (solid line in Fig. 3) from the IRAC Data Handbook reduces the peak-to-peak spread to 4.9% (filled circles).

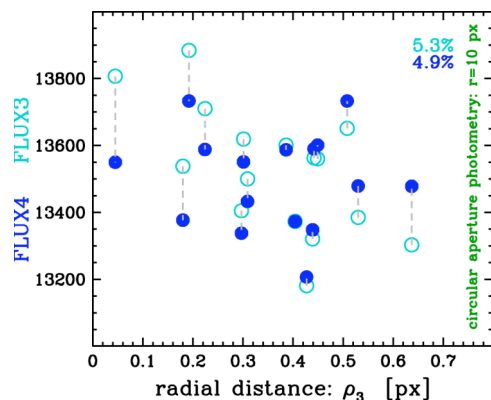


Fig. 4. Circular aperture photometry (radius of 10 pixels)

Hoping to improve the measurement by reducing the contribution of background noise, circular aperture photometry centered on the star with a radius of 5 pixels was done using the interactive “a” keyboard command of IRAF’s imexamine task. Fig. 5 shows a 4.5% peak-to-peak spread in the raw circular aperture flux measurements (open circles). Applying the recommended Ch1 flux correction (solid line in Fig. 3) from the IRAC Data Handbook reduces the peak-to-peak spread to 3.5% (filled circles).

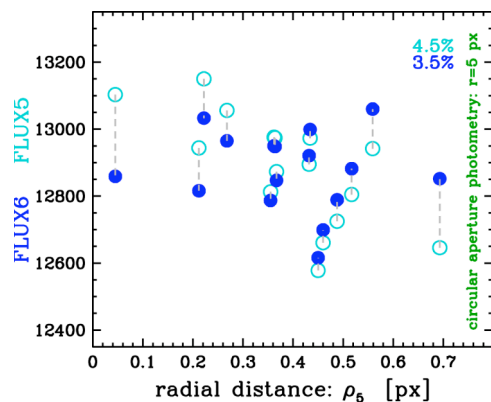


Fig. 5. Circular aperture photometry (radius of 10 pixels)

5. MATPHOT SIMULATIONS

Ten thousand IRAC Ch1 observations of a single star on a flat background were simulated and analyzed with MPDZ. Each stellar observation was simulated using the theoretical 5x5 supersampled IRAC Ch1 PSF shown in Fig. 1; a star with 10^6 electrons was located near the center of an field of 60x60 pixels on a flat background of 100 electrons. The horizontal axis of the left graph of Fig. 6 shows the subpixel offset (distance) the center of a star is from the middle of a pixel; stars centered near the middle of a pixel will have small offset values while stars located near the corner of a pixel will have offsets near 0.7 px. The vertical axis of the left graph of Fig. 6 shows the absolute flux ratio of the total fluxes divided by the true flux of 10^6 electrons. The cyan points show the *observed* absolute flux ratios and the blue points show the measured absolute flux ratios as reported by MPDZ. Note that

while the *average* stellar observation suffered an absolute flux loss of about 9%, stars centered near the middle of a pixel suffered, on average, an absolute flux loss of about 7% as compared to an absolute flux loss of about 11% for stars centered near a pixel corner. It is important to note that *the vertical scatter seen in the observed flux ratios is not random but systematic*; a simple radial correction function can only partially recover the lost flux. The *measured* absolute flux ratios are clustered around unity and are not a function of subpixel offset; the vertical scatter seen in the measured absolute flux ratios is random. By modeling the image formation process within the detector, MPDZ was able to fully recover all of the stellar flux lost due to the non-uniform IRAC Ch1 intrapixel quantum efficiency variations.

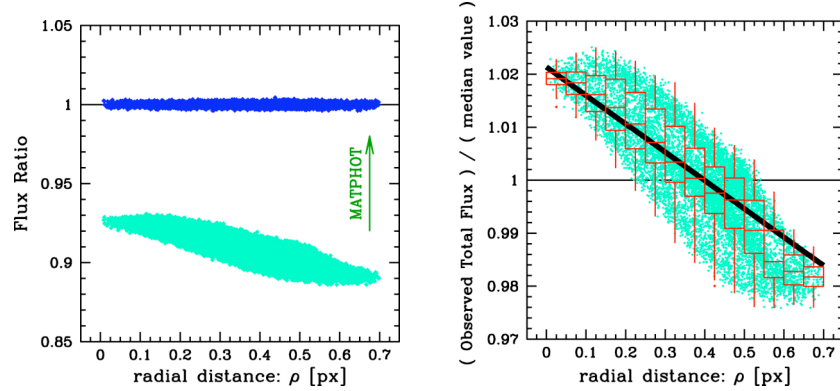


Fig. 6. Results of the MPDZ experiment with simulated IRAC Ch1

The vertical axis of the right graph of Fig. 6 shows the *observed* (apparent) total flux divided by the *median observed* total flux value of all ten thousand stars. The median values of the box-and-whisker plots (the central horizontal bar in each box) range from an excess flux of about 2% for stars centered near the center of a pixel to a flux deficit of about 2% for stars centered near the corner of a pixel. Note that this graph reproduces almost exactly the observed flux loss distribution seen in Fig. 5.1 of the IRAC Data Handbook [16]. One sees that even after the recommended flux correction (thick line of right graph of Fig. 6) is applied an approximate peak-to-peak spread of about 3% would remain for many observations – and that is exactly what is seen in Fig. 5.

6. MATPHOT PHOTOMETRY

MATPHOT PSF-fitting photometry was performed on all of the observations using MPDZ with the theoretical 5x5 supersampled IRAC Ch1 PSF shown in Fig. 1. The open diamonds in Fig. 7 show a 5.2% peak-to-peak spread in the raw measured stellar flux values reported by MPDZ.

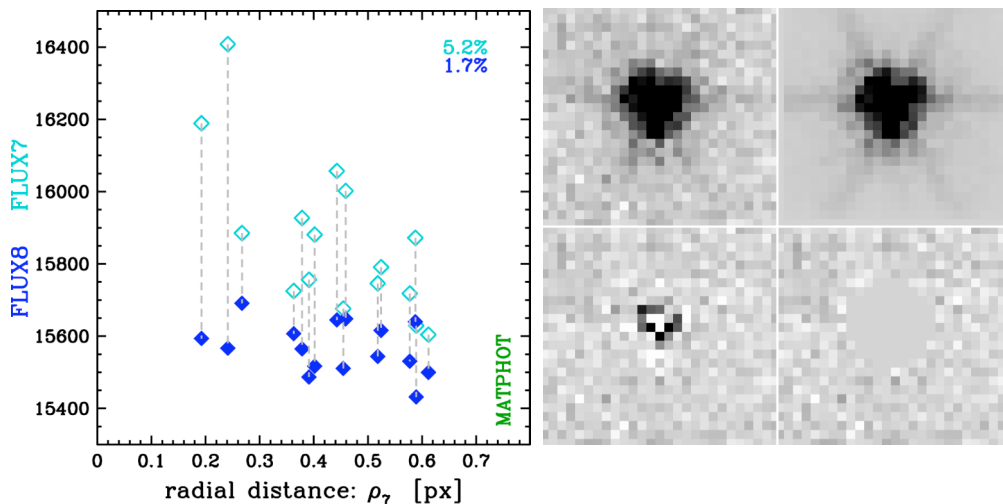


Fig. 7. MATPHOT (MPDZ) photometry

The upper-left image in Fig. 7 shows central portion of the first IRAC Ch1 observation in Table 1. The noiseless best-fit model of the observation is shown in the upper-right image. The residuals remaining after the best-fit model is subtracted from the observation are shown in the lower-left image. The lower-right image is the same as the residual image except that all residuals within a radius of 5 pixels from the fitted center of the star have been set to zero. All of these images are displayed with the same negative linear stretch which was chosen to emphasize the faint features of the stellar image.

The filled diamonds in Fig. 7 show a 1.7% peak-to-peak spread; these flux values are the combination of the raw measured stellar fluxes (open diamonds) with the sum of all of residuals (positive and negative) within a radius of 5 pixels from the fitted center of the star.

MATPHOT with residuals yield an improvement in photometric precision of more than 100% over the best results obtained with aperture photometry. The left graph of Fig. 8 compares MATPHOT photometry with residuals (FLUX8: filled diamonds in Fig. 7) with the best corrected circular photometry (FLUX6: filled circles in Fig. 5). The errorbars plotted with the FLUX8 values are the errors estimated by MPDZ for the raw MATPHOT flux estimates (FLUX7: open diamonds in Fig. 7).

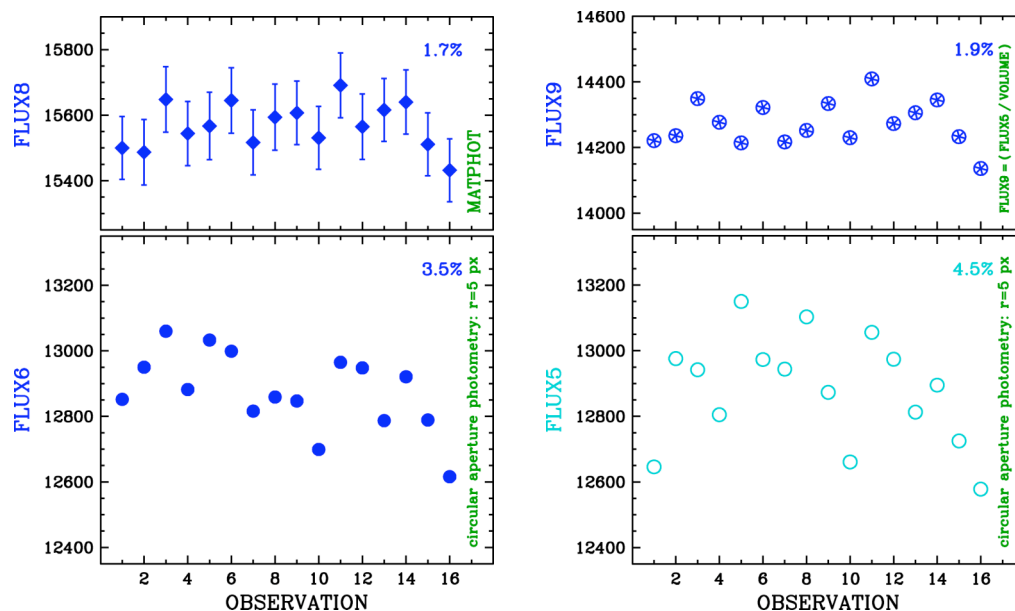


Fig. 8. Comparison between MATPHOT and aperture photometry

We see that although the recorded flux of point sources was corrupted by using lossy detectors with large intrapixel quantum efficiency variations, it is possible to significantly improve the precision of stellar photometry from observations made with such detectors – if the image formation process inside the detector is accurately modeled.

Simple aperture photometry of stellar observations obtained with IRAC Ch1 can be significantly improved by simply dividing the measured aperture flux with the volume of the Point Response Function (PRF) which is the convolution of the Point Spread Function and the discrete Detector Response Function. The right graph of Fig. 8 compares the best uncorrected circular photometry (FLUX5: open circles in Fig. 5) with those flux values divided by the volume of the best-fit PRF computed by MPDZ. The resultant peak-to-peak spread is 1.9% which is just slightly worse than the 1.7% spread from the MATPHOT with residual results. This suggests that aperture photometry from IRAC Ch1 observations could probably be significantly improved by using a two-dimensional correction function instead of using the radial correction function currently recommended in the IRAC Data Handbook. The derivation of that two-dimensional correction function would require a detailed analysis of a large number of dithered IRAC Ch1 unsaturated stellar observations.

7. SUMMARY AND DISCUSSION

This detailed analysis of multiple observations of a single bright isolated star obtained with Channel 1 of the *Spitzer Space Telescope*'s Infrared Array Camera (IRAC) instrument yields an improvement in photometric precision of more than 100% over the best results obtained with aperture photometry. The improvement is achieved by accurately modeling the image formation process within lossy detectors that exhibit large intrapixel quantum efficiency variations.

Mitigating the impact of flux loss problems seen in state-of-the-art NASA-grade infrared detectors is still in its early days. Hoffmann's IRAC Ch1 intrapixel QE map [14] is the *first attempt* by the IRAC team to quantify this effect. Derivation of the intrapixel QE map is an *iterative process* due to the apparent centroid shifting caused by the non-uniform QE variation across a pixel; given an initial estimate of the intrapixel QE map, better positions of the input stellar images can then be determined, which, in turn, enables a better measurement of the intrapixel QE map to be made

Much more work remains to be done. However, the possibility of significantly improving the precision and accuracy of space-based near-infrared stellar photometry and astrometry appears to be excellent. Ground-based infrared stellar photometry can typically achieve 10% accuracy and 5% accuracy under excellent conditions; the *Spitzer Space Telescope* is currently achieving only 5% photometry despite the fact that it is a cold stable observing platform in deep space. A significant improvement to 2% photometric accuracy might now be possible with image analysis software that models the image formation process within the detector. A stretch goal of 1% photometric accuracy may even be achievable with *existing* space-based cameras using state-of-the-art near-infrared detector technology – if onboard cameras are electronically quiet and stable enough.

I wish to thank Bill Glaccum, Bill Hoffmann, David Elliott, Patrick Lowrance, and the rest of the IRAC team for their support of this research effort. This work has been supported by a grant from the National Aeronautics and Space Administration (NASA), Interagency Order No. NNG06EC81I, which was awarded by the Applied Information Systems Research (AISR) Program of NASA's Science Mission Directorate.

8. REFERENCES

1. Mighell, K. J., Stellar photometry and astrometry with discrete point spread functions, *MNRAS*, Vol. 361, 861-878, 2005
2. Kernighan, B. W. and Ritchie, D. M., *The C Programming Language* (2nd Edition), Prentice Hall, New Jersey, 1988.
3. Hanisch, R. J., et al., Definition of the Flexible Image Transport System (FITS), *A&A*, Vol. 376, 359-380, 2001.
4. Mighell, K. J., MATPHOT algorithm for digital point spread function CCD stellar photometry, *Astronomical Data Analysis II*, Proceedings of the SPIE, Vol. 4847, 207-216, 2002.
5. Mighell, K. J., The MATPHOT Algorithm for Digital Point Spread Function CCD Stellar Photometry, *Astronomical Data Analysis Software and Systems XI*, ASP Conf. Ser. 281, 387-391, 2002.
6. All source code and documentation at the MATPHOT website at NOAO:
<http://www.noao.edu/staff/mighell/matphot>
7. Levenberg, K., A Method for the Solution of Certain Problems in Least Squares, *Quarterly of Applied Mathematics*, Vol. 2, 164-168, 1944.
8. Marquardt, D., Marquardt, An Algorithm for Least-Squares Estimation of Nonlinear Parameters, *SIAM Journal of Applied Mathematics*, Vol. 11, 431-441, 1963.
9. Mighell, K. J., Accurate stellar photometry in crowded fields, *MNRAS*, Vol. 238, 807-833, 1989.
10. Mighell, K. J., Algorithms for CCD Stellar Photometry, *Astronomical Data Analysis Software and Systems VIII*, ASP Conf. Ser. 172, 317-328, 1999.
11. Fazio, G. G., The Infrared Array Camera (IRAC) for the Spitzer Space Telescope, *ApJS*, Vol. 154, 10-17, 2004.
12. Tody, D., The *IRAF* Data Reduction and Analysis System, *Instrumentation in Astronomy VI*, Proceedings of the SPIE, Vol. 627, 733, 1986.

13. Tody, D., IRAF in the Nineties, *Astronomical Data Analysis Software and Systems II*, ASP Conf. Ser. 52, 173, 1993.
14. Hoffmann, B., Intra-pixel Variation Effect on Aperture Photometry, IRAC/TMo5-028 (Simfit Report 59; Version 2: December 10, 2005), 2005.
15. Hoffmann, B., 25 Position Model Pixel Repsonse Functions (PRF) Description and Quality, IRAC/TMo5-014 Simfit Report 52; September 3, 2005), 2005.
16. Reach, W. T., et al., Infrared Array Camera Data Handbook (Version 3.0; January 20, 2006), 2006.

The Lost Flux Method: A New Algorithm for Improving the Precision of Space-Based Near-Infrared Stellar Photometry with Lossy Detectors

Kenneth J. Mighell

National Optical Astronomy Observatory, Tucson, AZ, USA

Abstract. Current infrared detector technology can produce imagers with non-uniform intra-pixel response functions. Cameras based on such detectors can have large systematic errors in the measurement of the total stellar flux. Although this problem can be mitigated by oversampling the stellar image, many near-infrared cameras are undersampled in order to achieve a large field of view. The combination of undersampling stellar images with non-uniform detectors is currently diminishing some of the potential science return of some infrared imagers onboard the *Hubble Space Telescope* and the *Spitzer Space Telescope*. Although the recorded flux and position of point sources is corrupted by using detectors with non-uniform intrapixel response functions, it is still possible to achieve excellent stellar photometry and astrometry—if the image formation process inside the detector is accurately modeled. A new analysis algorithm called the *Lost Flux Method* is described and used to demonstrate how the precision of stellar photometry from an existing space-based near-infrared camera with a lossy detector can be significantly improved. Multiple observations of a single bright isolated star obtained with Channel 1 of the *Spitzer Space Telescope* Infrared Array Camera (IRAC) instrument are analyzed with the Lost Flux Method which yields an improvement in photometric precision of more than 100% over the best results obtained with aperture photometry.

1. Photometry and Astrometry with Discrete PSFs

The MATPHOT algorithm for precise and accurate stellar photometry and astrometry with discrete (sampled) Point Spread Functions (PSFs) was described in detail by Mighell (2005). The current C-language implementation of the MATPHOT algorithm works with user-provided discrete PSFs consisting of a numerical table represented by a matrix in the form of a FITS image (Hanisch et al. 2001). Discrete PSFs are shifted within an observational model using a 21-pixel-wide damped sinc function and position partial derivatives are computed using a five-point numerical differentiation formula. Precise and accurate stellar photometry and astrometry are achieved with undersampled charge coupled device (CCD) observations by using supersampled discrete PSFs that are sampled 2, 3, or more times more finely than the observational data. Although these numerical techniques are not mathematically perfect, they are sufficiently accurate

for precision stellar photometry and astrometry due to photon noise which is present in all astronomical imaging observations. The current photometric reduction code¹ is based on a robust implementation of the Levenberg-Marquardt method of nonlinear least-squares minimization (Levenberg 1944; Marquardt 1963; Mighell 1989, 1999). Detailed analysis of simulated *James Webb Space Telescope* observations demonstrate that millipixel relative astrometry and millimagnitude photometric precision should be achievable with complicated space-based discrete PSFs (Mighell 2005).

2. Observations and Photometric Reductions

Sixteen short (0.4 s) calibration observations of the K0-class star PPM 9412 (a.k.a. HIP 6378) were obtained² on 2003 October 8 UT with Channel 1 (3.6 μm) of the Infrared Array Camera (IRAC; Fazio et al. 2004) on-board the *Spitzer Space Telescope*. The IRAC basic calibrated data (BCD) images were retrieved from the *Spitzer* data archive with the kind assistance of IRAC team member B. Glaccum. These observations were analyzed with the *imexamine* task of NOAO's Image Reduction and Analysis Facility (IRAF; Tody 1993 and references therein) package and a new experimental version of MATPHOT, called MPDZ, which uses the following relative intrapixel quantum efficiency (QE) variation map for IRAC Channel 1 (Ch1),

$$\text{intrapix} = \begin{pmatrix} 0.813 & 0.875 & 0.875 & 0.875 & 0.813 \\ 0.875 & 1.000 & 1.000 & 1.000 & 0.875 \\ 0.875 & 1.000 & 1.000 & 1.000 & 0.875 \\ 0.875 & 1.000 & 1.000 & 1.000 & 0.875 \\ 0.813 & 0.875 & 0.875 & 0.875 & 0.813 \end{pmatrix}$$

(Hoffmann 2005a), and a theoretical IRAC Ch1 PSF for the central region of IRAC Ch1 (Hoffmann 2005b). MATPHOT models the image formation process within the detector by convolving the PSF with the discrete Detector Response Function (DRF) which, in this case, is based on the relative intrapixel QE map given above.

3. Square Aperture Photometry

Square aperture photometry with a 21×21 pixel box centered on the star was done using the interactive “m” keyboard command of IRAF's *imexamine* task. A 5.6% peak-to-peak spread was seen in these square aperture flux measurements. A non-random variation in flux is quite apparent in these 16 IRAC Ch1 observations: the total stellar flux measured is strongly correlated with the amount of flux found in the central pixel. Examination of the individual observations revealed that the observations with the most stellar flux have stellar images that

¹All source code and documentation for MATPHOT is available at this website: <http://www.noao.edu/staff/mighell/matphot>

²Observations: ads/sa.spitzer#00068nnnnn where nnnnn is 75392, 76672, 76928, 77184, 77440, 77696, 77952, 78208, 78464, 78720, 78976, 79232, 79488, 79744, 80000, 80256.

are centered in the middle of a pixel while those observations with the least stellar flux are centered on a pixel corner. This effect, shown graphically in Fig. 5.1 of the IRAC Data Handbook, is due to the combination of large quantum efficiency variations within individual pixels and the undersampling of the PSF by the DRF, is most severe in Channel 1 ($3.6\ \mu\text{m}$) where the correction can be as much as 4% peak to peak (Reach et al. 2006).

4. Circular Aperture Photometry

Circular aperture photometry centered on the star with a radius of 10 pixels was done using the interactive “a” keyboard command of IRAFs *imexamine* task. A 5.3% peak-to-peak spread was seen in the raw circular aperture flux measurements. Applying the recommended Ch1 flux correction from the IRAC Data Handbook (Reach et al. 2006) only slightly reduces the peak-to-peak spread to 4.9%. Reducing the aperture radius to just 5 pixels does improve the photometric precision; a 4.5% peak-to-peak spread was seen in the raw circular aperture flux measurements which reduces to 3.5% when the recommended Ch1 flux correction was applied. This is the best that aperture photometry can do with these observations.

5. MATPHOT Photometry

MATPHOT PSF-fitting photometry was performed on all of the observations using MPDZ with a theoretical 5×5 supersampled IRAC Ch1 PSF kindly provided by IRAC team member B. Hoffmann (see Hoffmann 2005b). The raw measured stellar flux values reported by MPDZ had a 5.2% peak-to-peak spread. However, when those flux values are combined with the sum of all of the residuals (positive and negative differences between the data and the best-fit model) within a radius of 5 pixels from the fitted center of the star, then the photometry has a 1.7% peak-to-peak spread—an improvement in photometric precision of more than 100% over the best results obtained with aperture photometry (see left graph of Figure 1). This experiment has demonstrated that even if the recorded flux of point sources is corrupted by using lossy detectors with large intrapixel quantum efficiency variations, it is practical to significantly improve the precision of stellar photometry from observations made with such detectors by accurately modeling the image formation process within the detector.

A very interesting finding of this experiment is that simple aperture photometry of stellar observations obtained with IRAC Ch1 can be significantly improved by simply dividing the measured aperture flux with the MPDZ-computed volume of the Point Response Function (PRF) which is the convolution of the PSF with the discrete DRF. When the best *uncorrected* circular aperture flux values were divided by the volume of the best-fit PRF computed by MPDZ, the photometric precision improved from the 4.5% peak-to-peak value (reported above) to just 1.9% (see right graph of Figure 1) which is just slightly worse than the 1.7% spread result from MPDZ with residuals. This suggests that aperture photometry from IRAC Ch1 observations could probably be significantly improved by using a two-dimensional correction function instead of using the radial correction function currently recommended in the IRAC Data Hand-

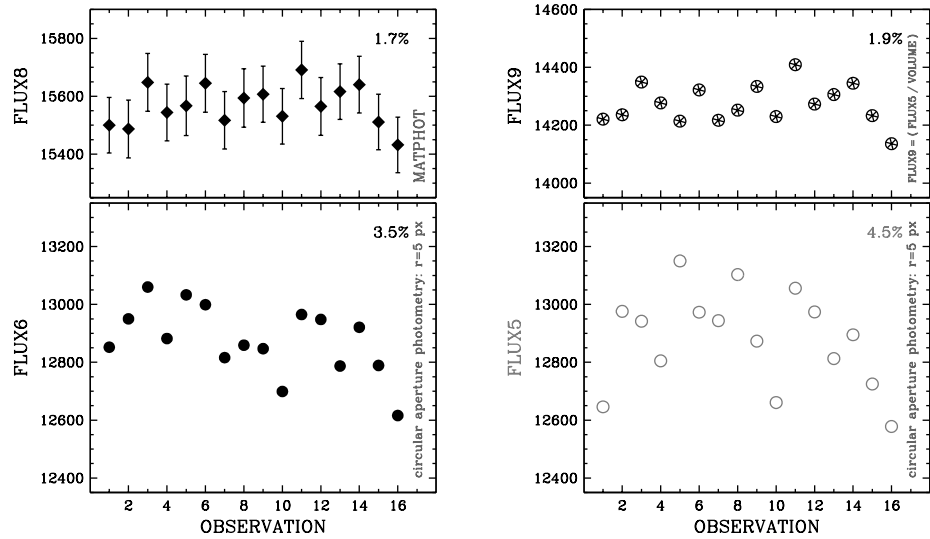


Figure 1. MATPHOT (MPDZ) photometry with residuals versus circular aperture photometry with a radius of 5 pixels.

book. The derivation of that two-dimensional correction function would require a detailed analysis of a large number of dithered IRAC Ch1 unsaturated stellar observations.

Acknowledgments. I wish to thank B. Glaccum, W. Hoffmann, D. Elliott, P. Lowrance, and the rest of the IRAC team for their support of this research effort. This work has been supported by a grant from the National Aeronautics and Space Administration (NASA), Interagency Order No. NNG06EC81I, which was awarded by the NASA Applied Information Systems Research Program.

References

- Fazio, G. G., et al. 2004, *ApJS*, 154, 10
- Hanisch, R. J., et al. 2001, *A&A*, 376, 359
- Hoffmann, B. 2005a, IRAC/TMo5-028 (Pasadena, CA: Spitzer Space Telescope)
- Hoffmann, B. 2005b, IRAC/TMo5-014, (Pasadena, CA: Spitzer Space Telescope)
- Levenberg, K. 1944, *Quarterly of Applied Mathematics*, 2, 164
- Marquardt, D. 1963, *SIAM Journal of Applied Mathematics*, 11, 431
- Mighell, K. J. 1989, *MNRAS*, 238, 807
- Mighell, K. J. 1999, in *ASP Conf. Ser.*, Vol. 172, ADASS VIII, ed. D. M. Mehringer, R. L. Plante, & D. A. Roberts (San Francisco: ASP), 317
- Mighell, K. J. 2005, *MNRAS*, 361, 861
- Reach, W. T., et al. 2006, *Infrared Array Camera Data Handbook*, Vers. 3.0 (Pasadena, CA: Spitzer Space Telescope)
- Tody, D. 1993, in *ASP Conf. Ser.*, Vol. 52, ADASS II, ed. R. J. Hanisch, R. J. V. Brissenden, & J. Barnes (San Francisco: ASP), 173

[Smithsonian/NASA ADS Astronomy Abstract Service](#)

- [Find Similar Abstracts](#) (with [default settings below](#))
- [Also-Read Articles](#) ([Reads History](#))
- [Translate Abstract](#)

Title: The Lost Flux Method: A New Algorithm for Improving the Precision of Space-Based Near-Infrared Stellar Photometry with Lossy Detectors

Authors: [Mighell, Kenneth J.](#)

Affiliation: AA(NOAO)

Publication: 2007 AAS/AAPT Joint Meeting, American Astronomical Society Meeting 209, #164.14

Publication Date: 12/2006

Origin: AAS

Abstract Copyright: (c) 2006: American Astronomical Society

Bibliographic Code: 2006AAS...20916414M

Abstract

The combination of undersampling stellar images with detectors that have non-uniform pixel response functions is currently diminishing the science return of some near-infrared imagers onboard the Hubble Space Telescope and the Spitzer Space Telescope. Although the recorded flux of point sources may vary significantly by using detectors with large effective intrapixel quantum efficiency variations, it is still possible to achieve excellent stellar photometry -if the image formation process inside the detector is accurately modeled. A new analysis technique called the Lost Flux Method is described and used to demonstrate how the precision of stellar photometry from an existing space-based near-infrared camera with a lossy detector can be significantly improved. A detailed analysis of multiple observations of a single bright isolated star obtained with Channel 1 of the Spitzer Space Telescope Infrared Array Camera (IRAC) instrument yields an improvement in photometric precision of more than 100% over the best results obtained with aperture photometry. This work has been supported by a grant from the National Aeronautics and Space Administration (NASA), Interagency Order No. NNG06EC81I, which was awarded by the Applied Information Systems Research (AISR) Program of NASA's Science Mission Directorate.

[Bibtex entry for this abstract](#) [Preferred format for this abstract](#) (see [Preferences](#))

Add this article to private library

Remove this article from private library

Find Similar Abstracts:

Use: ☐ Authors
☒ Title

☒ Abstract TextReturn: ☐ Query Results Return items starting with number ☐ Query FormDatabase: ☒ Astronomy☐ Physics☐ arXiv e-prints

[Smithsonian/NASA ADS Homepage](#) | [ADS Sitemap](#) | [Query Form](#) | [Basic Search](#) | [Preferences](#) | [HELP](#) | [FAQ](#)

The Lost Flux Method: A New Algorithm for Improving the Precision of Space-Based Near-Infrared Stellar Photometry with Lossy Detectors

Kenneth Mighell
National Optical Astronomy Observatory
mighell@noao.edu

ABSTRACT

The combination of undersampling stellar images with detectors that have non-uniform pixel response functions is currently diminishing the science return of some near-infrared imagers onboard the Hubble Space Telescope and the Spitzer Space Telescope. Although the recorded flux of point sources may vary significantly by using detectors with large effective intrapixel quantum efficiency variations, it is still possible to achieve excellent stellar photometry – if the image formation process inside the detector is accurately modeled. A new analysis technique called the Lost Flux Method is described and used to demonstrate how the precision of stellar photometry from an existing space-based near-infrared camera with a lossy detector can be significantly improved. A detailed analysis of multiple observations of a single bright isolated star obtained with Channel 1 of the Spitzer Space Telescope Infrared Array Camera (IRAC) instrument yields an improvement in photometric precision of more than 100% over the best results obtained with aperture photometry.

Observations and Photometric Reductions

Sixteen short (0.4 s) calibration observations of the K0-class star PPM 9412 (a.k.a. HIP 6378) were obtained on 2003 October 8 UT with Channel 1 (3.6 μm) of the Infrared Array Camera (IRAC; Fazio et al. 2004) onboard the *Spitzer Space Telescope*. The IRAC basic calibrated data (BCD) images were retrieved from the *Spitzer* data archive with the kind assistance of IRAC team member Bill Glaccum. These observations were analyzed with the *imexamine* task of NOAO's IRAF package and a new experimental version of MATPHOT (Mighell 2005), called MPDZ (Mighell 2006), which uses the following relative intrapixel quantum efficiency (QE) variation map for IRAC Channel 1 (Ch1),

$$\text{intrapix} = \begin{pmatrix} 0.813 & 0.875 & 0.875 & 0.875 & 0.813 \\ 0.875 & 1.000 & 1.000 & 1.000 & 0.875 \\ 0.875 & 1.000 & 1.000 & 1.000 & 0.875 \\ 0.875 & 1.000 & 1.000 & 1.000 & 0.875 \\ 0.813 & 0.875 & 0.875 & 0.875 & 0.813 \end{pmatrix}$$

(Hoffmann 2005a), and a theoretical IRAC Ch1 PSF for the central region of IRAC Ch1 (Hoffmann 2005b). MATPHOT models the image formation process within the detector by convolving the PSF (PSF) with the discrete Detector Response Function (DRF) which, in this case, is based on the relative intrapixel QE map given above.

ACKNOWLEDGEMENTS

I wish to thank B. Glaccum, B. Hoffmann, D. Elliott, P. Lowrance, and the rest of the IRAC team for their support of this research effort. This work has been supported by a grant from the National Aeronautics and Space Administration (NASA), Interagency Order No. NNG06C8H1, which was awarded by the Applied Information Systems Research (AISR) Program of NASA's Science Mission Directorate.

Square Aperture Photometry

Square aperture photometry with a 21×21 pixel box centered on the star was done using the interactive “m” keyboard command of IRAF's *imexamine* task. Fig. 1 shows a 5.6% peak-to-peak spread was seen in these square aperture flux measurements. A non-random variation in flux is quite apparent in these 16 IRAC Ch1 observations: the total stellar flux measured is strongly correlated with the amount of flux found in the central pixel.

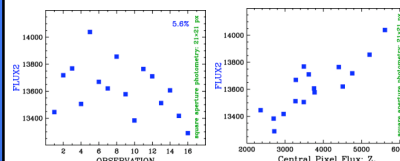


Figure 1. Square aperture photometry (21x21 pixels).

Examination of the individual observations revealed that the observations with the most stellar flux have stellar images that are centered in the middle of a pixel while those observations with the least stellar flux are centered on a pixel corner.

This effect, shown graphically in Fig. 5.1 of the IRAC Data Handbook (see Fig. 2), is due to the combination of large quantum efficiency variations within individual pixels and the undersampling of the Point Spread Function by the Detector Response Function, is most severe in Channel 1 (3.6 μm) where the correction can be as much as 4% peak to peak (Reach et al. 2006).

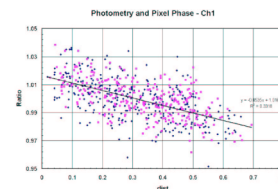


Figure 2. Normalized measured flux density (y-axis) is plotted against the distance of the source centroid from the center of a pixel (source: Fig. 5.1 of the IRAC Data Handbook).

Circular Aperture Photometry

Circular aperture photometry centered on the star with a radius of 10 pixels was done using the interactive “a” keyboard command of IRAF's *imexamine* task. A 5.3% peak-to-peak spread was seen in the raw circular aperture flux measurements. Applying the recommended Ch1 flux correction from the IRAC Data Handbook (Reach et al. 2006) only slightly reduces the peak-to-peak spread to 4.9%. Reducing the aperture radius to just 5 pixels does improve the photometric precision; a 4.5% peak-to-peak spread was seen in the raw circular aperture flux measurements which reduces to 3.5% when the recommended Ch1 flux correction was applied. This is the best that aperture photometry can do with these observations.

REFERENCES

- Fazio, G. G., et al., 2004, ApJS, 154, 10
- Reach, W. T., et al. 2006, Infrared Array Camera Data Handbook, Version 3.0 (Pasadena, CA: Spitzer Space Telescope)
- Hoffmann, B. 2005a, IRAC/TMo5-028 (Pasadena, CA: Spitzer Space Telescope)
- Hoffmann, B. 2005b, IRAC/TMo5-014, (Pasadena, CA: Spitzer Space Telescope)
- Mighell, K. J. 2005, MNRAS, 361, 861
- Mighell, K. J. 2006, Proc. SPIE, 6265, 6265T-1

MATPHOT Photometry

MATPHOT PSF-fitting photometry was performed on all of the observations using MPDZ with a theoretical 5×5 supersampled IRAC Ch1 PSF kindly provided by IRAC team member Bill Hoffmann (see Hoffmann 2005b). The raw measured stellar flux values reported by MPDZ had a 5.2% peak-to-peak spread.

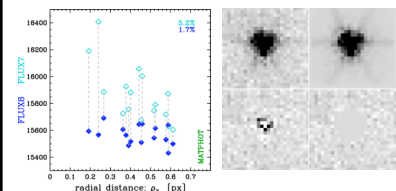


Figure 3. MATPHOT (MPDZ) photometry.

However, when those flux values are combined with the sum of all of the residuals (positive and negative differences between the data and the best-fit model) within a radius of 5 pixels from the fitted center of the star, then the photometry has a 1.7% peak-to-peak spread (see left graph of Fig. 3) — an improvement in photometric precision of more than 100% over the best results obtained with circular aperture photometry (see left graph of Fig. 4). This experiment has demonstrated that even if the recorded flux of point sources is corrupted by using lossy detectors with large intrapixel quantum efficiency variations, it is practical to significantly improve the precision of stellar photometry from observations made with such detectors by accurately modeling the image formation process within the detector.

A very interesting finding of this experiment is that simple aperture photometry of stellar observations obtained with IRAC Ch1 can be significantly improved by simply dividing the raw measured aperture flux with the MPDZ-computed volume of the Point Response Function (PRF) which is the convolution of the PSF with the discrete DRF. When the best uncorrected circular aperture flux values were divided by the volume of the best-fit PRF computed by MPDZ, the photometric precision improved from the 4.5% peak-to-peak value to just 1.9% (see right graph of Fig. 4) which is just slightly worse than the 1.7% spread result from MPDZ with residuals. This suggests that aperture photometry from IRAC Ch1 observations could probably be significantly improved by using a two-dimensional correction function instead of using the radial correction function currently recommended in the IRAC Data Handbook. The derivation of that two-dimensional correction function would require a detailed analysis of a large number of dithered IRAC Ch1 unsaturated stellar observations.

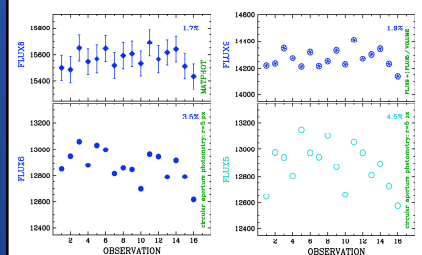


Figure 4. MATPHOT (MPDZ) photometry with residuals versus circular aperture photometry with a radius of 5 pixels.

Code Partitioning for Reconfigurable High-Performance Computing: A Case Study

Volodymyr Kindratenko

National Center for Supercomputing Applications (NCSA)

University of Illinois at Urbana-Champaign (UIUC)

kindr@ncsa.uiuc.edu

Abstract

In this case study, various ways to partition a code between the microprocessor and FPGA are examined. Discrete image convolution operation with separable kernel is used as the case study problem and SRC-6 MAPstation is used as the test platform. The overall execution time of the resulting implementation serves as the primary optimization criterion. The paper presents an overview of the SRC-6 architecture and programming tools and describes the case study problem, along with a timing analysis of its microprocessor-based implementation. Next, three code partitioning schemes are considered and their SRC-6 MAP implementations are described, including detailed timing analyses. The results are compared and conclusions are drawn as to what partitioning scheme characteristics contribute most to the reduction of the overall execution time of the algorithm. The results of this case study are applicable to a large class of problems that involve outsourcing computationally demanding tasks to a reconfigurable processor.

1. Introduction

Reconfigurable computing (RC) [1] based on field programmable gate array (FPGA) technology has the potential to yield performance improvements beyond those predicted by Moore's Law [2]. Recently introduced commercial high-performance reconfigurable computing (HPRC) systems, such as Cray XD1, SGI RASC, and SRC-6 MAPTM, which are based on the combination of conventional processors and FPGAs, enable software developers to exploit coarse-grain functional parallelism through conventional parallel processing as well as fine-grain parallelism through direct hardware execution on FPGAs. One of the key challenges in effectively using

these systems is the need for manual partitioning of the algorithm between the microprocessor(s) and FPGA(s). How to partition the code such that the best overall application performance can be achieved is a fundamental research question. While some work has been done on automatic code partitioning [3-5], none of the obtained results have been implemented on the current production systems, such as SRC-6 MAP. It is up to the software developer to analyze the code and decide what should be ported to the FPGA and what should be left on the microprocessor.

Some well-understood common metrics, such as the number of operations and results per data unit, data reuse efficiency, data per latency, etc. [6], can be useful to guide the partitioning process. Yet there are other practical considerations, such as the number of times the FPGA function is called, the number of times the direct memory access (DMA) engine is invoked, and microprocessor data manipulation tasks, that may have an adverse effect on the overall algorithm performance. The goal of this case study is to examine what impact different code partitioning schemes, which are similar in the common metrics space [6] but differ in other ways, have on the overall algorithm performance.

The case study is based on an example of an image convolution algorithm that uses a separable convolution kernel. This particular algorithm enables us to consider three levels of code partitioning granularity. At the lowest level, only the core computational kernel is outsourced to the FPGA and the microprocessor is left to deal with the memory manipulation tasks. At the intermediate level, the algorithm is partitioned along the lines of two major computational tasks. And at the highest level, the entire algorithm is ported to the FPGA. These code partitioning schemes demonstrate the impact of different levels of partitioning granularity on the overall code performance and the FPGA code

complexity. The observations made in the paper are intended to serve as the guidelines that one might refer to when considering porting code to an RC platform.

SRC-6 MAP [7] was used in this case study as the target platform because it is one the most readily available production RC systems on the market. The development toolset, called Carte [8], also provides a clear path for code development on the FPGA as well as a convenient debugging and simulation environment.

2. Case study problem

The MATPHOT code [9] used in stellar photometry and astrometry is the application driver for this work. The core of the code is a discrete convolution operation that convolves a synthetic image with a 21 coefficient-wide damped sinc function, $\text{sinc}(x) = \sin(\pi x) / \pi x$, using a separable kernel. In MATPHOT, single precision floating point numerical resolution is required for both the synthetic image and damped sinc function.

The basic idea of image convolution is that a window of some finite size and shape, $h[k, l]$, is scanned across the image and the output pixel value is computed as the weighted sum of the input pixels, $a[m, n]$, where the weights are the values of the filter assigned to every pixel of the window:

$$a[m, n] \otimes h[k, l] = \sum_{i=0}^{k-1} \sum_{j=0}^{l-1} a[m+i, n+j] h[i, j]$$

The window with its weights is called the *convolution kernel*. The *per-pixel* computational complexity for a $K \times L$ convolution kernel is $O(KL)$.

If the convolution kernel $h[k, l]$ is *separable*, that is, if the kernel can be written as

$$h[k, l] = h_{\text{row}}[l] \bullet h_{\text{col}}[k]$$

then the convolution can be performed as follows:

$$a[m, n] \otimes h[k, l] = \sum_{i=0}^{k-1} \left\{ \sum_{j=0}^{l-1} a[m+i, n+j] h_{\text{row}}[j] \right\} h_{\text{col}}[i]$$

Thus, instead of applying one two-dimensional convolution kernel, it is possible to apply two one-dimensional kernels: the first one in the l direction and the second one in the k direction. This reduces the per-pixel computational complexity to $O(K+L)$.

Microcomputer implementation of the last equation is straightforward: For an $M \times N$ image, $a[m, n]$, a one-dimensional convolution with $h_{\text{row}}[l]$ kernel is performed for each row of pixels followed by a convolution with $h_{\text{col}}[k]$ kernel for each column:

```

2DCONVOLUTION(A, B, M, N, Hr, Hc, L, K)
1  for m ← 0 to M-1
2    for n ← 0 to N-1
3      R1[n] ← A[m, n]
4      R2 ← 1DCONVOLUTION(R1, N, Hr, L)
5      for n ← 0 to N-1
6        B[m, n] ← R2[n]
7    end
8  for n ← 0 to N-1
9    for m ← 0 to M-1
10     C1[m] ← B[m, n]
11     C2 ← 1DCONVOLUTION(C1, M, Hc, K)
12     for m ← 0 to M-1
13       B[m, n] ← C2[m]
14   end
15 return B

```

Here **A** denotes input image, **B** denotes output image, both of dimension $M \times N$, **Hr** denotes the convolution kernel (consisting of L elements) applied to each row, and **Hc** denotes the convolution kernel (consisting of K elements) applied to each column. Lines 1-7 correspond to per-row convolution: Pixels from each row are copied to a separate array (lines 2-3), **R1**, a one-dimensional convolution with the appropriate coefficients is performed on **R1** (line 4), and the results are copied to the destination image **B** (lines 5-6), which is then processed in a similar manner for each column (lines 8-14). Finally, the following is the 1DCONVOLUTION subroutine:

```

1DCONVOLUTION(I, O, P, H, Q)
1  for p ← 0 to P-1
2    O[p] ← 0
3    for q ← 0 to Q-1
4      O[p] ← O[p] + I[p+q] · H[q]
5  end
6  return O

```

The 2DCONVOLUTION algorithm is the subject of the present study. Its computational complexity is $O((K+L)MN)$; thus, for a fixed-size convolution kernel the overall execution time of the algorithm is the function of image size.

3. Case study platform

The SRC-6 MAPstation [7] used in the course of this study consists of a commodity dual-CPU Xeon

board, a MAP Series C processor, and an 8 GB common memory module, all interconnected with a 1.4 GB/s low-latency switch. The SNAP™ Series B interface board is used to connect the CPU board to the Hi-Bar switch. The SNAP plugs directly into the mother board's DIMM memory slot.

The MAP Series C processor module contains two user FPGAs, one control FPGA, and memory. There are six banks (A-F) of on-board memory (OBM); each bank is 64 bits wide and 4 MB deep for a total of 24 MB. The programmer is responsible for data transfer to and from these memory banks via SRC programming macros invoked from the FPGA application. There is an additional 4 MB of dual-ported memory dedicated solely to data transfer between the two FPGAs.

The two user FPGAs in the MAP Series C are Xilinx Virtex-II XC2V6000 FPGAs. Each FPGA contains 6 million equivalent logic gates, 144 dedicated 18x18 integer multipliers, and 324 KB of internal dual-ported block RAM (BRAM). These FPGA elements are not directly visible to the programmer but are interconnected appropriately as determined by the programmer's MAP C algorithm code, the SRC Carte programming environment tools, and the Xilinx FPGA place and route tools. The FPGA clock rate of 100 MHz is set by the SRC programming environment.

The Carte programming environment [8] for the SRC MAPstation is highly integrated, and all compilation targets are generated via a single makefile. The two main targets of the makefile are a debug version of the entire program and the combined microprocessor code and FPGA hardware programming files. The debug version is useful for code testing before the final time-intensive hardware place and route step. Either the Intel icc compiler or the gcc compiler can be used to generate both the CPU-only debug executable and the CPU-side of the combined CPU/MAP executable. The SRC MAP compiler is invoked by the makefile to produce the hardware description of the FPGA design for final combined CPU/MAP target executable. This intermediate hardware description of the FPGA design is passed to the Xilinx ISE place and route tools, which produces the FPGA bit file. Lastly, the linker is invoked to combine the CPU code and the FPGA hardware bit file(s) into a unified executable.

4. Code partitioning alternatives

The core of the computation is a fixed-width 21-coefficient 1D convolution operation that uses single

precision floating point arithmetic. XC2V6000 FPGA has enough hardware multipliers to implement just two such 21-coefficient-wide fully unrolled operations (42 single precision floating point multiplications and 40 additions in total) using SRC's reduced space multiply macros. Therefore, our ability to perform simultaneous convolution operations is limited by the available FPGA hardware resources to just two such operations.

Considering the *overall execution time* of the algorithm as the main efficiency criteria, and taking into account availability of FPGA resources, what is the most efficient way to partition the 2D CONVOLUTION algorithm between the microprocessor and MAP processor?

To answer this question, we examine several partitioning options and investigate their run-time behavior. Perhaps the simplest partitioning approach is to outsource the 1D CONVOLUTION algorithm alone. Alternatively, the entire convolution operation in one dimension can be implemented on MAP. And finally, the entire 2D CONVOLUTION algorithm can be ported to MAP. Note that these partitioning alternatives result in the same number of calculations to be performed on MAP, thus, they are similar in the sense of the common metrics used in [6] (with the exception of data reuse efficiency), yet they are very different as far as the number of times the MAP subroutine is called and the type and amount of memory manipulations with which the microprocessor is left.

4.1. Code partitioning choice # 1

It is natural to consider a partitioning scheme in which the 1D CONVOLUTION subroutine alone is outsourced to the MAP processor. An obvious advantage of this approach is its simplicity: One is concerned with only one row or column of image pixels at a time without explicitly distinguishing between them, which simplifies the data management aspects of MAP code implementation. The main disadvantage of this approach, of course, is the need to call the MAP-based 1D CONVOLUTION function multiple times, thus likely encountering some MAP function call overhead that may have an effect on the overall performance.

Porting 1D CONVOLUTION to MAP is straightforward. There is enough space and hardware multipliers on the MAP's primary FPGA chip to perform two sets of convolution calculations in parallel using SRC's floating point single precision smaller area macros. Therefore, the overall MAP code sequence deployed on just one chip is:

- If run the first time, DMA from main RAM convolution coefficients to OBM bank F
- Copy convolution coefficients from OBM bank F to on-chip registers
- DMA from the RAM pixel values to OBM bank A
- Do calculations using pixels from OBM bank A and storing results in OBM bank B
 - Bring in the next two pixel values from OBM bank A to the on-chip pixel registers
 - Shift the on-chip pixel registers by two pixels
 - Perform two parallel convolution calculations
 - Store two results in OBM bank B
- DMA to main RAM results from OBM bank B

The mapped and routed FPGA implementation of the 1D CONVOLUTION subroutine occupies all available SLICES and 91% of all available MULT18X18s on one MAP Series C processor's FPGA and meets timing requirements of 9.998 ns.

4.2. Code partitioning choice # 2

The next partitioning scheme is based on the observation that in the CPU implementation the entire image is located in a continuous memory array, one row of pixels after another. Therefore, it is straightforward to have access to the consecutive rows of image pixels without copying them to a separate array. Thus, the per-row convolution calculations for the entire image can be outsourced to MAP, literally by replacing lines 1-7 in the 2D CONVOLUTION algorithm with just one call to a MAP-based subroutine. Once all rows of the image are processed, the image data must be rearranged in the memory so that the columns occupy a continuous memory array, one column of pixels after another. Then the same MAP subroutine can be called on the rearranged image with the net effect of performing per-column convolution calculations. At the end, the pixels are moved back to their original locations. The overall MAP code sequence for this implementation is:

- DMA in convolution coefficients to OBM bank F
- Copy convolution coefficients from OBM bank F to on-chip registers
- For each row of image pixels
 - DMA in pixel values to OBM bank A
 - Do calculations using pixels from OBM bank A and storing results in OBM bank B
 - DMA out results from OBM bank B

Conceptually, the MAP subroutine of this implementation is very similar to the previous

implementation; we just augmented the previously written code with an extra loop responsible for bringing in and out the next row/column of data rather than leaving this to the microprocessor. The microprocessor code now is left with the extra work needed to rearrange the image data in memory.

This implementation occupies all available SLICES, some of which are packed with unrelated logic, and 95% of all available MULT18X18s on one MAP Series C processor's FPGA and meets timing requirements of 9.994 ns.

4.3. Code partitioning choice # 3

In this partitioning scheme, the entire 2D CONVOLUTION algorithm is ported to MAP. However, there are some difficulties with implementing this approach in practice. Note that the previous design occupied all available SLICES on the MAP Series C processor's FPGA, some of which were already packed with unrelated logic. Therefore, the primary FPGA is used to implement the calculations in one image dimension and the secondary FPGA is used to implement the calculations in the other image dimension. The intermediate image is stored in the on-board memory, which limits the size of the image that can be processed by this implementation to 12 MB. The primary FPGA MAP code sequence is:

- DMA in one set of convolution coefficients to OBM bank E
- DMA in the other set of convolution coefficients to OBM bank F
- Copy convolution coefficients from OBM bank F to on-chip registers
- DMA in input image to OBM banks A-C
- For each row of image pixels
 - Do calculations using pixel values from OBM banks A, B, and C and storing results in OBM banks D, E, and F
- Let other chip to do per-column calculations
- DMA out results from OBM banks A-C

The FPGA chips on the MAP processor operate in a master-slave mode. The secondary chip waits until the primary chip is done with the per-row calculations and only then performs per-column calculations. The secondary FPGA MAP code sequence is:

- Copy convolution coefficients from OBM bank E to on-chip registers
- Wait until the primary chip is done with per-row calculations

- For each column of image pixels
 - Do calculations using pixel values from OBM banks D, E, and F and storing results in OBM banks A, B, and C

This implementation occupies all available SLICES and over 95% of MULT18X18s on both chips and meets timing requirements of 9.995 ns. However, it took some effort to fine-tune the secondary FPGA design to fit on the chip and meet timing requirements.

5. Implementation results and discussion

Let us first examine the original microprocessor-only implementation described in Section 2. Figure 1 shows how the overall execution time changes as the image size increases. It also shows what fraction of time is spent due to memory copy operations (lines 2-3, 5-6, 9-10, 12-13 of the 2D CONVOLUTION algorithm) and due to the actual calculations (lines 4 and 11). Thus, for a 2,048x2,048 pixel image, memory copy operations are responsible for about 0.72 seconds, whereas actual convolution calculations take about 0.62 seconds. (Calculations reported in this paper were performed on a 2.8 GHz Intel dual-Xeon platform; code was compiled with the gcc 3.4.3 compiler using the O3 optimization level. The microprocessor “Read Time Stamp Counter” instruction (RDTSC) [10] was used to measure timing information.)

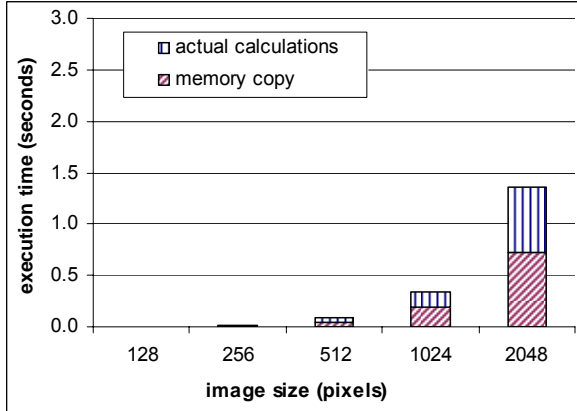


Figure 1. Time to compute vs. image size for 2D CONVOLUTION algorithm. The horizontal axis shows image dimensions, thus “512” means an image consisting of 512x512 pixels.

Figure 2 provides test results for the first partitioning scheme implemented as described in Section 4.1. As with the microprocessor-only implementation, a significant amount of time is spent

due to the memory copy operations, whereas time spent performing actual calculations is only marginally smaller than in the native CPU-only implementation. Note that ‘MAP code execution’ time includes both data transfer and convolution calculations time. However, an even larger amount of time is now spent due to the MAP function call overhead. We measure this overhead as the difference between the time spent on the CPU while executing the MAP function and the time measured inside the MAP function while executing its internals (including data transfer) on the FPGA. In other words, MAP function call overhead is what it takes to call an “empty” MAP function that returns immediately without any work done.

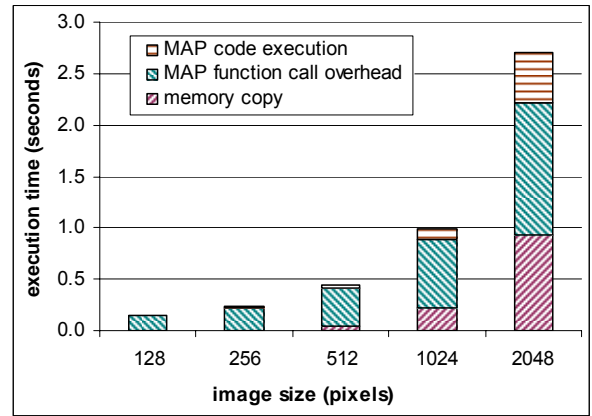


Figure 2. Execution time for 2D CONVOLUTION algorithm in which 1D CONVOLUTION subroutine alone is ported to MAP.

Figure 3 provides test results for the second partitioning scheme implementation described in Section 4.2. The MAP function call overhead, which was a major issue with the previous code partitioning scheme, is now independent of the image size (since the MAP function is called only twice) and became much smaller. The MAP code execution time increased as compared to the previous implementation. However, the amount of time spent due to the memory copy operations on the CPU remains about the same as with our previous implementation, even though each pixel value is copied only twice, whereas in the previous implementation it was copied four times, although in smaller memory segments. This is likely due to the CPU memory cache misses.

Note that the actual calculation time of the MAP implementation can still be reduced if we involve the second FPGA chip available on the MAP Series C processor. But even this will not reduce the overall algorithm execution time with any significance since the time spent due to the image rearrangement on the

CPU accounts for the majority of the execution time. The need to “rotate” the image twice in the system memory resulted in a significant time overhead.

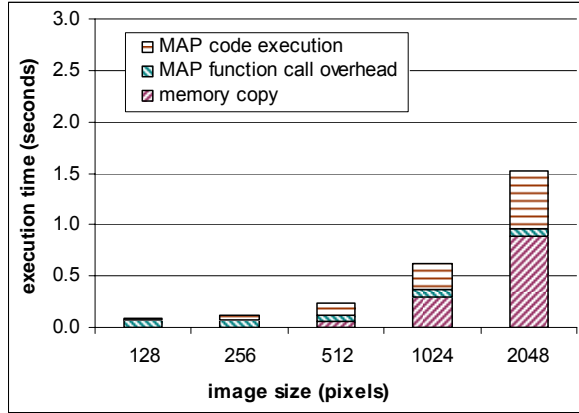


Figure 3. Execution time for 2D CONVOLUTION algorithm in which the entire convolution operation in one image dimension is outsourced to MAP.

Figure 4 provides test results for the third partitioning scheme implemented as described in Section 4.3. In this implementation, all the microprocessor-side calculations and memory manipulations have been eliminated. The MAP subroutine is called only once, therefore the MAP function call overhead remains small and independent of the image size. This overhead, however, is doubled as compared to the previous implementation due to the fact that now both FPGA chips are used. On the other hand, the actual calculation time measured on the MAP decreased significantly since the DMA engine is invoked from the FPGA design only twice, once to transfer in the entire image and once to transfer out. (Remember that in the previous implementation the DMA engine was invoked twice per each image row/column.) Thus, for an image consisting of 1,772x1,772 pixels, we achieved a 3x overall code execution speedup.

Figure 5 shows a combined comparison chart of the execution time for all four implementations. It is clear that the first code partitioning scheme suffers due to the MAP function call overhead. Even though this partitioning scheme is intuitive and simple to implement, it increases the overall execution time because the MAP function is called frequently and thus the accumulated MAP function call overhead adds up quickly to the overall execution time.

The second code partitioning scheme suffers due to the need to perform costly memory manipulations on the microprocessor and also due to the need to invoke the DMA data transfer engine multiple times.

The third code partitioning scheme eliminates the need for any memory manipulations on the microprocessor side. It also eliminates the need for the frequent use of the DMA data transfer engine as the entire image data is transferred in and out only once. As a result, the MAP code execution time is very short and the overall execution time is dominated by the MAP function call overhead.

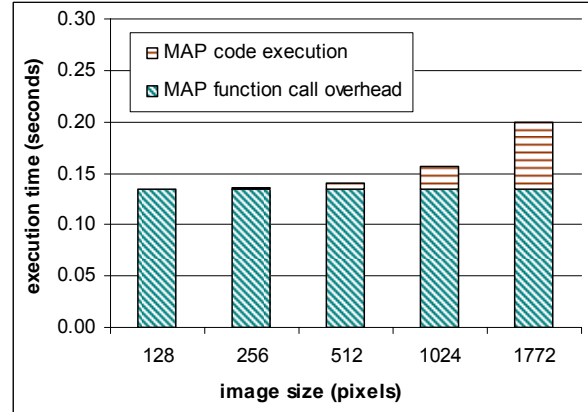


Figure 4. Execution time as a function of image size for 2D CONVOLUTION algorithm implemented solely on MAP. Note the vertical axis scale difference between this figure and Figures 1- 3. Also note that the largest image that can be processed by this implementation is 1,772x1,772 pixels.

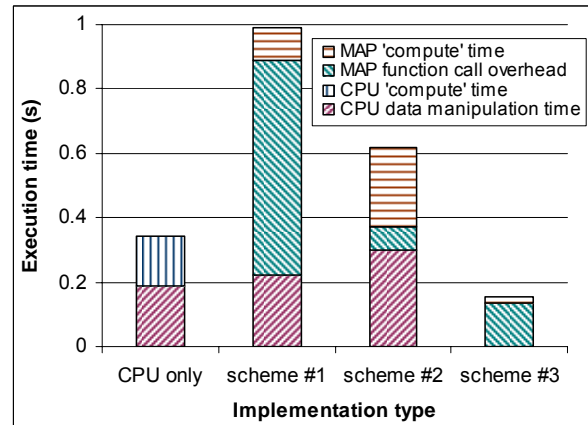


Figure 5. Execution time comparison chart for a 1,024x1,024 pixels image.

The 2D CONVOLUTION algorithm is an interesting case to study since the best way to partition it is not immediately clear based on the run-time analysis of the algorithm shown in Figure 1. It is tempting to port the 1D CONVOLUTION algorithm alone since it is responsible for about half of the overall execution time. Yet this resulted in a

significant MAP function call overhead that increased the overall execution time (Figure 2). Porting the entire 2D CONVOLUTION algorithm presents some challenges since it requires both MAP FPGAs to be utilized at their full capacity, thus making it difficult to meet timing requirements. Yet this approach yields the best overall performance.

6. Conclusions and future work

All three partitioning schemes presented in this paper resulted in the same number of calculations executed on the FPGA when combined across a single run of the 2D CONVOLUTION algorithm. Yet they resulted in very different execution times. This points out the importance of the overall code organization for reconfigurable system applications. The MAP function should be called as few times as possible in order to eliminate the MAP function call overhead. A partitioning scheme that reduces or eliminates the need for data manipulations by the microprocessor should be considered. The DMA engine should be invoked in the MAP code as few times as possible since it adds considerable overhead to the MAP code execution. Thus, when considering different code partitioning alternatives, in addition to the metrics based on various aspects of data reuse such as those reported in [6], one should also take into account other practical considerations, such as the number of times the MAP code will be invoked, amount of extra memory manipulation tasks left to the microprocessor, etc.

We have not seen MAP function call overhead timing measurements reported in the literature and our own estimates vary. For example, combined MAP function call overhead for the design described in Section 4.2 is 0.068 seconds, whereas the overhead for the design provided in Section 4.3 is 0.135 seconds. In the first case, only one FPGA chip was used and the MAP function was called twice. In the second case, both FPGAs were used, but the MAP subroutine was called only once. Our estimates show that the first time a MAP subroutine is called it encounters a 67 millisecond overhead due to the need to load the FPGA configuration bitfile. Each consecutive call to the same MAP function resulted in an overhead that varied for different designs. The nature of this variability and the ways it can be precisely measured and/or predicted is the subject of the future work.

7. Acknowledgements

This work was funded by the National Science Foundation (NSF) grant SCI 05-25308. MATPHOT

software was developed and kindly provided to us by Dr. Kenneth Mighell from the National Optical Astronomy Observatory. Special thanks to David Caliga, Dan Poznanovic, and Jeff Hammes, all from SRC Computers Inc., for their help and support with SRC-6 system. Further comments and suggestions were provided by David Pointer, Dr. Craig Steffen and David Raila from NCSA's Innovative Systems Laboratory. Special thanks to Trish Barker from NCSA's Office of Public Affairs for help in preparing this publication.

7. References

- [1] M.B. Gokhale, and P.S. Graham, *Reconfigurable Computing: Accelerating Computation with Field-Programmable Gate Arrays*, Springer, Dordrecht, 2005.
- [2] K. Underwood, "FPGAs vs. CPUs: Trends in Peak Floating Point Performance," In Proc. *12th ACM/SIGDA International Symposium on Field Programmable Gate Arrays*, Monterey, CA, 2004, pp 171-180.
- [3] T. Callahan, J. Hauser, and J. Wawrzynek, "The GARP architecture and C compiler". *IEEE Computers*, 33:4 (April 2000), pp. 62-69.
- [4] Y. Li, T. Callahan, E. Darnell, R. Harr, U. Kurkure, and J. Stockwood, "Hardware-software co-design of embedded reconfigurable architectures", In Proc. *Design Automation Conf.*, 2000, pp. 507--512.
- [5] B. Knerr, M. Holzer, and M. Rupp, "HW/SW Partitioning Using High Level Metrics", In Proc. *Int. Conf. on Computing, Communications and Control Technologies*, 2004, pp. 33-38.
- [6] V. Kindratenko, D. Pointer, and D. Caliga, "High-Performance Reconfigurable Computing Application Programming in C", *White Paper*, January 2006. netfiles.uiuc.edu/dpointer/www/whitepapers/hprc_v1_0.pdf
- [7] SRC Computers Inc., Colorado Springs, CO, *SRC Systems and Servers Datasheet*, 2005.
- [8] SRC Computers Inc., Colorado Springs, CO, *SRC C Programming Environment v 1.9 Guide*, 2005.
- [9] Mighell, K. J., "Stellar photometry and astrometry with discrete point spread functions", *Monthly Notices of the Royal Astronomical Society*, 316, 861-878 (11 August 2005).
- [10] *IA-32 Intel® Architecture Software Developer's Manual*, Volume 3B: System Programming Guide, Part 2.